



UvA-DARE (Digital Academic Repository)

A CHIME/FRB Study of Burst Rate and Morphological Evolution of the Periodically Repeating FRB 20180916B

Sand, K.R.; Breitman, D.; Michilli, D.; Kaspi, V.M.; Chawla, P.; Fonseca, E.; Mckinven, R.; Nimmo, K.; Pleunis, Z.; Shin, K.; Andersen, B.C.; Bhardwaj, M.; Boyle, P.J.; Brar, C.; Cassanelli, T.; Cook, A.M.; Curtin, A.P.; Dong, F.A.; Eadie, G.M.; Gaensler, B.M.; Kaczmarek, J.; Lanman, A.; Leung, C.; Masui, K.W.; Rahman, M.; Pandhi, A.; Pearlman, A.B.; Petroff, E.; Rafiei-Ravandi, M.; Scholz, P.; Shah, V.; Smith, K.; Stairs, I.; Stenning, D.C.

DOI

[10.3847/1538-4357/acf221](https://doi.org/10.3847/1538-4357/acf221)

Publication date

2023

Document Version

Final published version

Published in

Astrophysical Journal

License

CC BY

[Link to publication](#)

Citation for published version (APA):


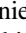
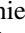

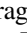



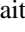
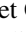


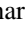
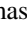
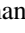


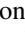
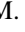


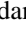
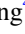

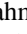
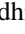
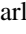
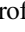
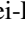
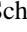
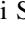



Sand, K. R., Breitman, D., Michilli, D., Kaspi, V. M., Chawla, P., Fonseca, E., Mckinven, R., Nimmo, K., Pleunis, Z., Shin, K., Andersen, B. C., Bhardwaj, M., Boyle, P. J., Brar, C., Cassanelli, T., Cook, A. M., Curtin, A. P., Dong, F. A., Eadie, G. M., ... Stenning, D. C. (2023). A CHIME/FRB Study of Burst Rate and Morphological Evolution of the Periodically Repeating FRB 20180916B. *Astrophysical Journal*, 956(1), Article 23. <https://doi.org/10.3847/1538-4357/acf221>

General rights

It is not permitted to download or to forward/distribute the text or part of it without the consent of the author(s) and/or copyright holder(s), other than for strictly personal, individual use, unless the work is under an open content license (like Creative Commons).



A CHIME/FRB Study of Burst Rate and Morphological Evolution of the Periodically Repeating FRB 20180916B

Ketan R. Sand^{1,2} , Daniela Breitman³ , Daniele Michilli^{4,5} , Victoria M. Kaspi^{1,2} , Pragma Chawla⁶ , Emmanuel Fonseca^{7,8} , Ryan Mckinven^{1,2} , Kenzie Nimmo⁴ , Ziggy Pleunis⁹ , Kaitlyn Shin^{4,5} , Bridget C. Andersen^{1,2} , Mohit Bhardwaj¹⁰ , P. J. Boyle^{1,2} , Charanjot Brar^{1,2} , Tomas Cassanelli¹¹ , Amanda M. Cook^{9,12} , Alice P. Curtin^{1,2} , Fengqiu Adam Dong¹³ , Gwendolyn M. Eadie^{12,14} , B. M. Gaensler^{9,12,22} , Jane Kaczmarek^{15,16} , Adam Lanman^{1,2} , Calvin Leung^{4,5,21} , Kiyoshi W. Masui^{4,5} , Mubdi Rahman¹⁷ , Ayush Pandhi^{9,12} , Aaron B. Pearlman^{1,2} , Emily Petroff¹⁸ , Masoud Rafiei-Ravandi^{1,2} , Paul Scholz^{9,19} , Vishwangi Shah^{1,2} , Kendrick Smith¹⁸ , Ingrid Stairs¹³ , and David C. Stenning²⁰ 

¹ Department of Physics, McGill University, 3600 rue University, Montréal, QC, H3A 2T8, Canada; ketan.sand@mail.mcgill.ca

² Trotter Space Institute, McGill University, 3550 rue University, Montréal, QC, H3A 2A7, Canada

³ Scuola Normale Superiore, Piazza dei Cavalieri 7, I-56126 Pisa, Italy

⁴ MIT Kavli Institute for Astrophysics and Space Research, Massachusetts Institute of Technology, 77 Massachusetts Avenue, Cambridge, MA 02139, USA

⁵ Department of Physics, Massachusetts Institute of Technology, 77 Massachusetts Avenue, Cambridge, MA 02139, USA

⁶ Anton Pannekoek Institute for Astronomy, University of Amsterdam, Science Park 904, 1098 XH Amsterdam, The Netherlands

⁷ Center for Gravitational Waves and Cosmology, West Virginia University, Chestnut Ridge Research Building, Morgantown, WV 26505, USA

⁸ Department of Physics and Astronomy, West Virginia University, P.O. Box 6315, Morgantown, WV 26506, USA

⁹ Dunlap Institute for Astronomy & Astrophysics, University of Toronto, 50 St. George Street, Toronto, ON, M5S 3H4, Canada

¹⁰ Department of Physics, Carnegie Mellon University, 5000 Forbes Avenue, Pittsburgh, PA 15213, USA

¹¹ Department of Electrical Engineering, Universidad de Chile, Av. Tupper 2007, Santiago 8370451, Chile

¹² David A. Dunlap Department of Astronomy & Astrophysics, University of Toronto, 50 St. George Street, Toronto, ON, M5S 3H4, Canada

¹³ Department of Physics and Astronomy, University of British Columbia, 6224 Agricultural Road, Vancouver, BC, V6T 1Z1 Canada

¹⁴ Department of Statistical Sciences, University of Toronto, 700 University Avenue 9th Floor, Toronto, ON, M5G 1X6, Canada

¹⁵ CSIRO Space and Astronomy, Parkes Observatory, P.O. Box 276, Parkes NSW 2870, Australia

¹⁶ Department of Computer Science, Math, Physics and Statistics, University of British Columbia, Kelowna, BC, V1V 1V7, Canada

¹⁷ Sidrat Research, 124 Merton Street, Suite 507, Toronto, ON, M4S 2Z2, Canada

¹⁸ Perimeter Institute for Theoretical Physics, 31 Caroline Street N, Waterloo, ON, N2S 2YL, Canada

¹⁹ Department of Physics and Astronomy, York University, 4700 Keele Street, Toronto, ON, M3J 1P3, Canada

²⁰ Department of Statistics and Actuarial Science, Simon Fraser University, 8888 University Drive, Burnaby, BC, V5A 1S6, Canada

Received 2023 July 11; revised 2023 August 8; accepted 2023 August 10; published 2023 October 4

Abstract

FRB 20180916B is a repeating fast radio burst (FRB) with a 16.3 day periodicity in its activity. In this study, we present morphological properties of 60 FRB 20180916B bursts detected by CHIME/FRB between 2018 August and 2021 December. We recorded raw voltage data for 45 of these bursts, enabling microseconds time resolution in some cases. We studied variation of spectro-temporal properties with time and activity phase. We find that the variation in dispersion measure (DM) is $\lesssim 1 \text{ pc cm}^{-3}$ and that there is burst-to-burst variation in scattering time estimates ranging from ~ 0.16 to over 2 ms, with no discernible trend with activity phase for either property. Furthermore, we find no DM and scattering variability corresponding to the recent change in rotation measure from the source, which has implications for the immediate environment of the source. We find that FRB 20180916B has thus far shown no epochs of heightened activity as have been seen in other active repeaters by CHIME/FRB, with its burst count consistent with originating from a Poissonian process. We also observe no change in the value of the activity period over the duration of our observations and set a 1σ upper limit of $1.5 \times 10^{-4} \text{ day day}^{-1}$ on the absolute period derivative. Finally, we discuss constraints on progenitor models yielded by our results, noting that our upper limits on changes in scattering and DM as a function of phase do not support models invoking a massive binary companion star as the origin of the 16.3 day periodicity.

Unified Astronomy Thesaurus concepts: [Radio transient sources \(2008\)](#); [Radio bursts \(1339\)](#)

1. Introduction

Fast radio bursts (FRBs) are microsecond to millisecond duration radio pulses of extragalactic origins (see Bailes 2022;

Petroff et al. 2022 for a recent review on FRBs). Their properties have inspired numerous theories to explain their origin (see Platts et al. 2019 for review²³). A bright radio burst detected from SGR J1935+2154 (CHIME/FRB Collaboration et al. 2020a; Bochenek et al. 2020) in 2020 April suggests that magnetars are likely progenitors for some of these sources. Some FRBs are seen to repeat, i.e., multiple bursts from the same source. After the publication of the Canadian Hydrogen Intensity Mapping Experiment/Fast Radio Bursts (CHIME/FRB) first catalog (CHIME/FRB Collaboration et al. 2021),

²¹ NHFP Einstein Fellow.

²² Present address: Division of Physical and Biological Sciences, University of California Santa Cruz, Santa Cruz, CA 95064, USA.



Original content from this work may be used under the terms of the [Creative Commons Attribution 4.0 licence](#). Any further distribution of this work must maintain attribution to the author(s) and the title of the work, journal citation and DOI.

²³ https://frbtheorycat.org/index.php/Main_Page

the number of published FRBs has surpassed over 600, out of which 51 show repeat bursts (CHIME/FRB Collaboration et al. 2019; Fonseca et al. 2020; CHIME/FRB Collaboration et al. 2023) in subsequent observations.

FRB 20180916B is one of the first repeating sources discovered by the CHIME/FRB collaboration (CHIME/FRB Collaboration et al. 2019), who later showed it exhibits a 16.33 day periodicity in its activity (CHIME/FRB Collaboration et al. 2020b). It has been localized to a nearby spiral galaxy approximately 150 Mpc away by Marcote et al. (2020). The source is active for approximately 5 days in its 16.33 day cycle (CHIME/FRB Collaboration et al. 2020b). This activity is frequency dependent, with higher-frequency detections occurring at earlier phases (Pastor-Marazuela et al. 2021; Pleunis et al. 2021). The source has been detected over a wide frequency range, from 110 MHz by the Low-Frequency Array (LOFAR; Pastor-Marazuela et al. 2021; Pleunis et al. 2021; Gopinath et al. 2023) to 6 GHz by the Effelsberg telescope (Bethapudi et al. 2023) at different activity phases. This chromatic periodicity has led to multiple progenitor scenarios involving precessing (e.g., Li & Zanazzi 2021), rotating (e.g., Beniamini et al. 2020), or binary systems (e.g., Wada et al. 2021). The first repeating source, FRB 20121102A, has also shown a tentative activity period of around 160 days (Rajwade et al. 2020; Cruces et al. 2021).

Understanding the evolution of source properties with time can help further narrow down the models capable of explaining the activity period and emission origins. The distinctive ability of CHIME/FRB to monitor the entire Northern sky at a daily cadence makes it an ideal instrument for such a study. Rotation measure (RM) variation has been observed for FRB 20121102A over 2.5 yr, decreasing by almost 34% its initial value (Michilli et al. 2018; Hilmarsson et al. 2021). This variation was accompanied by a 4 pc cm^{-3} increase in the dispersion measure (DM). The RM of FRB 20180916B is 4 orders of magnitude less than that of FRB 20121102A and was fairly stable until 2021 April. Mckinven et al. (2023) reported a linear increase in the RM of FRB 20180916B in their recent CHIME/FRB polarimetric data analysis. No significant DM changes have been observed for the source so far. Gopinath et al. (2023) also observed these changes at LOFAR frequencies (150 MHz). This suggests a change in the magnetic field environment in the source proximity that is independent of the mechanism causing the periodic activity.

Scattering is another crucial property useful in understanding the source environment. Most FRB scattering times are longer than what is expected from their Galactic contribution (Cordes et al. 2016; Cordes & Chatterjee 2019). Chawla et al. (2022) showed that scattering in FRBs is likely due to their more extreme circumburst environments compared to those of pulsars in the Galactic plane. Contributions from the circumgalactic medium of intervening galaxies can also add to the total measured scattering (Vedantham & Phinney 2019). FRB 20180916B has a low Galactic latitude, and most of its scattering, as determined using scintillation bandwidth measurements, has been attributed to the Milky Way (Marcote et al. 2020; Bethapudi et al. 2023). However, bursts with scattering tails considerably longer than the expected value from the Milky Way interstellar medium (ISM) have been observed in low-frequency observations, suggesting possible contributions from the immediate source environment (Pleunis et al. 2021; Sand et al. 2022; Gopinath et al. 2023). Thus, understanding

the long-term and phase-dependent variation in scattering behavior of the source can in principle help better characterize its immediate environment.

Repeating FRBs tend to have complex burst morphologies (CHIME/FRB Collaboration et al. 2019; Fonseca et al. 2020; CHIME/FRB Collaboration et al. 2023). In particular, the downward-drifting “sad trombone” effect is a characteristic feature of their dynamic spectra (Hessels et al. 2019; Pleunis et al. 2021). This may sometimes prevent the accurate estimation of both DM and scattering values. FRB 20180916B exhibits microstructure at 1.7 GHz as narrow as $3 \mu\text{s}$ (Nimmo et al. 2021) and down to 800 MHz as narrow as $30 \mu\text{s}$ (Sand et al. 2022). Such structures might remain hidden at lower time resolution and can contaminate scattering estimates. Moreover, studying such structures can constrain the source’s emission models. Microstructures as narrow as 60 ns have been seen for FRB 20200120E (Nimmo et al. 2022) at 1.4 GHz and at 2.3 GHz (Majid et al. 2021), suggesting a magnetically powered emission mechanism that can generate energies comparable to FRBs at $\lesssim \mu\text{s}$ timescales. Past studies in the CHIME band (CHIME/FRB Collaboration et al. 2020b; Pleunis et al. 2021) of this source have had insufficient time resolution to detect microstructure. FRB 20180916B’s less-turbulent immediate environment compared to other active repeaters such as FRB 20121102A (Spitler et al. 2014, 2016) makes it an ideal source for such a study. Identifying microsecond variations in the burst envelope to accurately estimate the DM and scattering requires high time resolution, available only with raw voltage data that can be coherently dedispersed. By “raw voltage” we mean the complex voltage induced by the incoming electromagnetic radiation in the telescope feed. This allows us to extract phase information. We can then use this to completely remove the effects of dispersion by coherent dedispersion to our best estimate of DM. The CHIME/FRB baseband system (CHIME/FRB Collaboration et al. 2018; Michilli et al. 2021) provides such functionality, enabling the comprehensive study of these ultra-fast emissions on a population scale and for individual repeating sources down to $2.56 \mu\text{s}$.

Repetition rates of repeaters are useful in understanding their activity, which can give clues into possible progenitors. For example, a rate of more than 100 bursts per hour has been observed for FRB 20121102A (Li et al. 2021a) at 1.3 GHz. Such high rates put limits on the energy budget of the source. Sources like FRB 20201124A (Lanman et al. 2022) and FRB 20220912A (Mckinven & CHIME/FRB Collaboration 2022) have shown sudden activity with repetition rates of tens to hundreds of bursts per hour, respectively. Although transiting daily in the CHIME/FRBs field of view, no burst above our detection threshold had been detected from these sources despite a lot of exposure before their heightened activity periods. FRB 20180916B, on the other hand, has been detected continuously at the expected period since its discovery by CHIME/FRB in 2018. However, a comprehensive study on the evolution of its long-timescale emission rate until now has only been done at LOFAR frequencies (Gopinath et al. 2023).

Here we present a morphology analysis of 45 bursts from FRB 20180916B detected by the CHIME/FRB baseband system from its first detection in 2018 September 16 to 2021 December 31. We use the same baseband burst sample published by Mckinven et al. (2023), where they report the polarization properties. In addition, we present burst properties

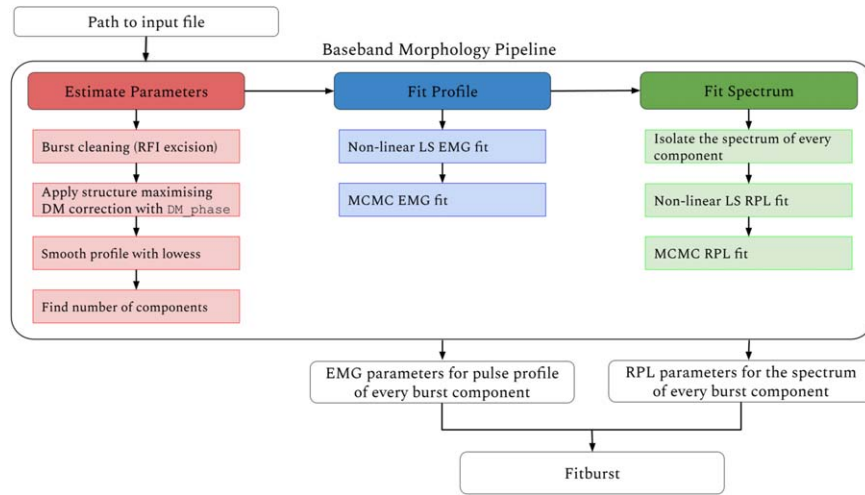


Figure 1. Flowchart showing the Baseband Morphology Pipeline. The path on the left involves extracting the Stokes intensity (I) data products from the beamformed file, dedispersing and cleaning the spectra, getting the burst profile and estimating the number of subbursts/peaks to fit for. The middle portion indicates the process of extracting initial guesses on the temporal profile of each subburst, first by a least-squares (LS) fit and then by Markov Chain Monte Carlo (MCMC) sampling using an exponential modified Gaussian (EMG). As indicated in the right-hand column we then estimate the spectral parameters using the same methods assuming a running power-law (RPL) model. The resulting data file along with initial guesses are then provided to `fitburst`.

for 15 bursts that have been detected only with intensity data since the last published results for the source (Pleunis et al. 2021). We also analyze the evolution of the burst rate of the source and the burst count distribution with respect to its activity cycles in the aforementioned date range. In Section 2, we provide a brief outline of CHIME/FRB and the CHIME/FRB baseband system used for our observations. In Section 3, we present the analysis and the results, providing a detailed outline of our Baseband morphology pipeline. In Section 4, we discuss the implications of our results. Lastly, we provide concluding remarks in Section 5.

2. Observations

CHIME is an array of four stationary cylinders, each $100\text{ m} \times 20\text{ m}$ in dimensions, located near Penticton, British Columbia. Along the axis of each cylinder are hung 256 equispaced feeds recording dual polarization in the frequency range 400–800 MHz for the overhead sky (CHIME Collaboration et al. 2022). The system was designed to map the distribution of neutral hydrogen in the redshift range 0.8–2.5 (Amiri et al. 2023). However, its daily Northern sky coverage and high sensitivity make it an excellent FRB detection machine.

The CHIME/FRB backend uses the CHIME telescope to search for FRBs in real time as the sky transits (CHIME/FRB Collaboration et al. 2018). This process involves a comprehensive set of stages, from radio frequency interference (RFI) cleaning (Rafiei-Ravandi & Smith 2022) to dedispersion, beam grouping, known source sifting, and finally, data callbacks for signals deemed astrophysical. The system stores intensity data for all FRB sources at a resolution of 0.983 ms and 16384 frequency channels (i.e., 24.4 kHz in frequency resolution). A detailed analysis of 536 of these sources was published by CHIME/FRB Collaboration et al. (2021). Optimized for FRB searching, this system is restricted in time resolution and does not store polarization information.

For this reason, CHIME/FRB has a separate triggered baseband system (CHIME/FRB Collaboration et al. 2018). This system records buffered raw voltage data when an FRB is

detected above a specified signal-to-noise ratio (S/N) threshold. The system has a data buffer of 20 s, permitting the recording of CHIME’s full bandwidth for a DM of up to 1000 pc cm^{-3} . This allows us to coherently dedisperse the voltage data around the detected DM and study the bursts at a time resolution of $2.56\text{ }\mu\text{s}$. More details on the pipeline can be found in Michilli et al. (2021). The baseband data also permit analysis of Stokes parameters and extraction of polarization information, the specifics of which have been presented by Mckinven et al. (2021).

In this study, all 45 baseband bursts from FRB 20180916B were beamformed at the published VLBI position of the source (Marcote et al. 2020). Additionally, there are 15 bursts with only total intensity data. These were mostly low-S/N and hence did not trigger the baseband system.

3. Analysis and Results

All of the new bursts in our data set were identified using the clustering algorithm described by CHIME/FRB Collaboration et al. (2023). Among the baseband burst sample, we re-analyze the morphological properties of 21 previously published bursts (CHIME/FRB Collaboration et al. 2020b; Pleunis et al. 2021). The remaining 24 bursts in the sample are new detections.

We show our burst sample and tables with measured properties in the Appendix.

3.1. Baseband Morphology Pipeline

The baseband morphology pipeline is designed to fit a model to the data with morphological parameters such as burst width, scattering, bandwidth, arrival time, and DM from bursts detected by the baseband system. This pipeline interacts with Stokes intensity (I) data products in the final beamformed file, and a single tied-array beam is formed at the best known sky position of the given source (Michilli et al. 2021, 2023).

The pipeline has three main parts. See Figure 1 for a graphical representation of the pipeline workflow.

The first part starts with performing RFI excision using the functionalities described by Michilli et al. (2021). The burst is then dedispersed at its structure-maximizing DM, calculated

using the `DM_phase` package (Seymour et al. 2019). The pulse profile is then smoothed by applying locally weighted scatterplot smoothing (LOWESS) implemented by `statsmodels` (Seabold & Perktold 2010). LOWESS is a nonparametric regression method that weights a data neighborhood with some kernel. Thus, the only parameter it requires is the neighborhood size for smoothing, also known as the smoothing fraction. A small neighborhood will smooth very little, while a large neighborhood will smooth a lot. The pipeline typically uses a neighborhood size of 1.5%–20% of the profile estimated using an algorithm that considers burst properties such as S/N, time resolution, and pulse width. This smoothed profile is then used to estimate the number of burst components using `find_peaks` implemented by `SciPy` (Virtanen et al. 2020).

The second step focuses on getting initial guesses for the burst profile and its spectrum. We fit a sum of exponentially modified Gaussians (EMGs) to the entire burst profile (McKinnon 2014), with one term per subburst i , and with the scattering timescale fixed for all subbursts. We define the EMG as follows:

$$\begin{aligned} \text{EMG}(x; A_i; \mu_i; \sigma_i; \tau) &= \sum_{i=1}^N A_i \frac{1}{2\tau} \exp\left(\frac{1}{2\tau} \left(2\mu_i + \frac{\sigma_i}{\tau} - 2x\right)\right) \\ &\cdot \text{erfc}\left(\frac{\mu_i^2 + \frac{\sigma_i^2}{\tau} - x}{2\sqrt{\sigma_i}}\right), \end{aligned} \quad (1)$$

where x is the input time series, A is the amplitude, μ is the Gaussian mean, σ is the variance, and τ is the scattering timescale for each of the N components.

The 1D spectrum of each subburst is fit with a running power law (RPL) defined as follows:

$$\text{RPL}_i(f; A_i; r_i; \gamma_i) = A_i (f/f_o)^{-\gamma_i + r_i \ln(f/f_o)}, \quad (2)$$

where f_o is an arbitrary reference frequency chosen to be the middle of the band at 600 MHz, r is the spectral running, and γ is the spectral index. The spectral model is identical to the one described by CHIME/FRB Collaboration et al. (2021).

Using these models, first, a nonlinear least-squares algorithm `curve_fit` from `SciPy` is used to get initial conditions for the steps (*walkers*) of each of the Markov Chains. A Markov Chain Monte Carlo (MCMC) sampling algorithm is then implemented using the `emcee` routine (Foreman-Mackey et al. 2013) using independent wide uniform prior distributions for all parameters. We use a chi squared log-likelihood function. The MCMC process is quite fast (up to a few minutes, depending on the time resolution of the data); therefore, it can be easily run multiple times until the posterior has converged. However, note that this depends on the quality of the data being fit. Very low-S/N data may not converge quickly, in which case, we would increase the downsampling factor (i.e., reduce the time resolution) in order to increase the S/N. Once the downsampling has been increased enough, we can adjust the chain length and number of walkers to convergence.

In the third and final step, the EMG and RPL fit parameters obtained for the time series and the spectrum, respectively, are passed on to `fitburst`, which performs a 2D fit on the data set, as described in the following section.

3.1.1. *Fitburst*

`Fitburst` is a least-squares optimization routine that models the burst morphology and dynamic spectrum. The model includes all of the fundamental burst parameters: DM, the time of arrival (t_{arr}) in the given data file, the signal amplitude (A), temporal width (σ), power-law spectral index (γ), “running” of the spectral index (r), and scattering timescale of the signal (τ). For a signal with N components, the DM and scattering timescale are set to be the same for each of the subbursts, with $2 + 5N$ parameters being fitted through χ^2 optimization. The resulting mathematical formulation can be found in CHIME/FRB Collaboration et al. (2021).

The routine computes a noise-weighted fit residual using the following equation:

$$h_{t,f}(\lambda) = \frac{d_{t,f}}{\sigma_f} - S_{t,f}(\lambda). \quad (3)$$

Here, $d_{t,f}$ is the data as a function of discrete time and frequency channel, λ is the set of fit parameters described above, σ_f is the standard deviation in the noise calculated for each frequency channel, and $S_{t,f}$ is the model. `Fitburst` then employs the `optimize.least_squares` functionality of `scipy` to minimize $\chi^2(\lambda) = \sum_{t,f} [h_{t,f}(\lambda)]^2$ with respect to model parameters. The uncertainties on the resulting fit parameters are computed using the covariance in the resulting χ^2 fit provided by the solver. This involves a Jacobian matrix comprised of partial derivatives of the fit equation at the minimized fit parameter values. More information about `fitburst` can be found in CHIME/FRB Collaboration et al. (2021) and Pleunis et al. (2021). A more detailed description will be forthcoming (E. Fonseca et al. 2023, in preparation), along with a public release of the codebase.

We report morphological parameters for the intensity and baseband bursts using `fitburst`, the only difference between the two being that the initial guesses for DM, burst width, etc. for the intensity burst fits are computed using the methodology described by CHIME/FRB Collaboration et al. (2021). For baseband bursts, we do not keep the DM fixed at its structure-maximizing value during fitting by `fitburst` but rather permit an offset in DM, making it a free parameter. This was done to obtain an optimized model for the burst parameters. We report this optimized value in Table 1.

3.2. Simulations

To obtain robust uncertainty estimates, we undertook simulations to better characterize the fitting results from `fitburst` for all of the baseband bursts. These simulations consisted of synthetic bursts generated using the `simpulse`²⁴ routine (Merryfield et al. 2023). The spectro-temporal properties of the simulated bursts mimic the measured parameters (see Table 1). For each of the 45 bursts, we generated 50 synthetic bursts each integrated into an array of random noise. `fitburst` was then run on the entire sample, and the measured value for each successful run was saved. We calculated the standard deviations of the measured parameters and then calculated the relative uncertainty with respect to simulated values. Finally, we scaled the error measurements in scattering and width for every burst in our sample by the

²⁴ <https://github.com/kmsmith137/simpulse>

relative uncertainty computed from the simulations. We repeated the entire process three times to verify our results. This yielded robust uncertainties, resulting in better characterization of the temporal evolution of morphological properties as described below.

3.3. Period and Period Derivative Analysis

We recalculated the activity period of FRB 20180916B using the arrival time of the new detections presented here and the updated exposure. The total on-sky exposure of the source from 2018 August 28 to 2021 December 31 was computed using the procedure described by CHIME/FRB Collaboration et al. (2021). In summary, we record metrics that indicate the variation in up-time and sensitivity of the CHIME/FRB system for the given interval. These metrics are combined with the beam model²⁵ to generate exposure maps, which we query at the VLBI position of the source (Marcote et al. 2020). Note that we only calculate exposure if the sky location lies within the FWHM of the beam at 600 MHz. The total exposure on the source in the aforementioned time interval is 201 hr, in which we detected 94 bursts.

We used the Pearson χ^2 test described by CHIME/FRB Collaboration et al. (2020b) to estimate the best period. The updated period is 16.34 ± 0.07 days, assuming the period derivative to be zero. We have used this period in all of our phase calculations. The source period has thus not changed prior to 2021 December 31 and is similar to the one reported by CHIME/FRB Collaboration et al. (2020b) and Pleunis et al. (2021). To constrain the period derivative, we modified our phase calculation term as follows:

$$\phi = \frac{t - t_o}{P} + \frac{1}{2} \left(\frac{-\dot{P}}{P^2} \right) (t - t_o)^2, \quad (4)$$

where ϕ is the phase, t_o is the reference Modified Julian Date (MJD; in this case 58369.40), P is the period, and \dot{P} is the period derivative. We then calculate χ^2 values again for each period and period derivative combination. Figure 2 shows our χ^2 distribution, and we perform a 2D Gaussian fit on it using the `Astropy` package. In this way, we find $P = 16.34 \pm 0.32$ days and $\dot{P} = -0.2 \pm 1.5 \times 10^{-4}$ day day⁻¹. This is consistent with the derivative being zero. The above analysis used eight phase bins, but we find similar order-of-magnitude results for up to 200 bins. Longer-term monitoring may eventually reveal a nonzero \dot{P} .

3.4. Burst Rate Analysis

Next we perform an analysis of the rate of bursts from FRB 20180916B in the CHIME band. After excising the bursts detected during days of low sensitivity and those detected outside the FWHM at 600 MHz, we are left with 40 bursts in our rate analysis.

The exposure for each activity cycle was calculated by folding the daily exposure data using a period of 16.34 days. We have had 74 activity cycles since the source’s discovery in 2018 September up to the end of 2021. Figure 3 (left) shows the burst count in each cycle. To test whether the counts are consistent with being drawn from a Poissonian distribution, we used a Kolmogorov–Smirnov (K-S) test (Massey 1951) and an

Anderson–Darling (A-D) test (Scholz & Stephens 1987). Figure 3 (right) shows the frequency distribution of the counts in dark green. We simulated 10,000 instances of a Poisson process, assuming a mean rate equal to the observed mean count of bursts, 1.27 events per activity period. We performed a K-S and A-D test for each distribution with our observed count distribution. Our median p -values, 0.512 (K-S) and 0.12 (A-D), show that the observed counts distribution is consistent with being Poissonian at 95% confidence.

We then estimated the burst rate for each activity cycle, as shown in Figure 4. There, error bars represent 95% confidence uncertainties assuming a Poissonian process within each cycle. As the telescope sensitivity varies across cycles, the rate for each cycle is scaled to a fluence threshold of 5.2 Jy ms by using an index of $\gamma = -2.3$ (CHIME/FRB Collaboration et al. 2020b). This threshold was calculated using the methodology described by Josephy et al. (2019). We see that the source’s activity is consistent with a single Poisson rate throughout the 3 yr of this study. The mean rate throughout the observation period is $0.2_{-0.1}^{+0.1}$ bursts per hour.

The rate distribution with respect to phase is shown in Figure 5. We divide the active phase into three subintervals. The rate centered around the peak activity of the source (0.45–0.55) is $0.86_{-0.35}^{+0.5}$ burst per hour at a fluence threshold of 5.2 Jy ms. However, the differences are not statistically significant with rates during earlier phases (0.35–0.45) of $0.82_{-0.35}^{+0.51}$ or later phases (0.55–0.65) of $0.24_{-0.16}^{+0.33}$ burst per hour. We might observe significant differences in phase-dependent rates with more detections in the future.

3.5. Evolution of Properties

Figure 6 shows the evolution of various spectro-temporal properties of the source with respect to MJD and to the phase of the 16.34 day cycle for all of the baseband bursts in our data set. The color scale shows the resolution at which we measured the burst’s morphological properties. The side-panel histogram presents the overall distribution. Only the bursts from the baseband sample were used in this analysis, as their spectral and temporal properties are better constrained.

Mckinven et al. (2023) reported a systematic linear increase in RM from this source (see Figure 6, third panel). However, interestingly, we do not find corresponding changes in any other source parameter.

We performed an augmented Dickey Fuller (ADF) test on DM values to test the time dependence. The ADF estimates a regression equation and checks if the regression coefficient applied to a lagged time series variable is significantly different from unity (Dickey & Fuller 1979). It tests the null hypothesis that a time series is nonstationary. With a p -value of $\sim 10^{-8}$, we find the DM is stationary and see no clear evolution with time, even during the corresponding RM evolution. The DM of the brightest burst in our data set, B35, is 348.81 ± 0.01 pc cm⁻³, which is 0.04 pc cm⁻³ greater than what was reported by Nimmo et al. (2021; 348.772 ± 0.001 pc cm⁻³). The DM we measure for different bursts requiring lower time resolution can be affected by underlying unresolved structure. We constrain the DM variation to $\lesssim 1$ pc cm⁻³.

The scattering timescale shows significant variation from burst to burst. However, in our ADF test, we do not observe any trend in this variation (p -value $\sim 10^{-10}$). We also do not see any phase dependence. Similarly, the widths also show stochastic variation with no particular trend, with the broadest

²⁵ <https://chime-frb-open-data.github.io/beam-model/>

burst being 6 ms. However, there are caveats regarding our measurements: weaker bursts are at lower time resolution. For bursts B4–B5 and B10–B11 (see Table 1), we see significant changes in the scattering value within the same CHIME transit. However, the bursts are not bright enough to resolve structures narrower than $\sim 160 \mu\text{s}$, which could affect our scattering estimates. Such sudden changes have also been claimed for FRB 20190520B (Ocker et al. 2023) and have been attributed to fluctuations in the turbulence in proximity to the circumburst environment.

In terms of spectral properties, we find that most of the bursts are narrowband, as is also seen for all other repeaters (Kumar et al. 2021; Pleunis et al. 2021). The average bandwidth in the CHIME band is ~ 150 MHz, with the narrowest case being 40 MHz. Some bursts were detected at the top or bottom of the CHIME band, so we cannot estimate their true bandwidth. However, for this source, we have not yet observed any multiband detection even after ~ 70 hr of observation (Pastor-Marazuela et al. 2021; Sand et al. 2022; Trudu et al. 2023). The central emission frequency of the bursts in our sample is distributed across the CHIME band, and there is no obvious correlation between the phase and emitting frequency. With more bursts in the future, we may be able to detect chromaticity as a function of phase in the CHIME band.

We also performed a structure-function analysis similar to the one presented by Mckinven et al. (2023) for scattering, in order to search for preferred timescales for variation. We find no measurable trend at any timescale, suggesting that the variations are random and occur due to fluctuations in the propagation environment.

3.6. Microstructure Analysis

Some FRBs have shown temporal microstructure. For FRB 20180916B, we have seen structures as narrow as $3 \mu\text{s}$ at 1.7 GHz (Nimmo et al. 2021) and $30 \mu\text{s}$ at 800 MHz (Sand et al. 2022). The bursts need to be coherently dedispersed and bright enough at finer time resolution for such narrow structure to be detectable. We selected 11 bursts from our data that were visible at a resolution of $80 \mu\text{s}$ or less (maximum downsample of 32; Table 1).

We analyzed the burst structure using a temporal auto-correlation function (ACF). First, we summed over the subbands in which the burst was detected. We then performed the ACF in time of the pulse profile of these bursts. We flagged the zero-lag peak, which inhibits the detection of narrow features in the ACF. We performed a Lorentzian fit on the wider burst envelope, which in this case corresponds roughly to the width of the burst.

Only one of the bright bursts showed interesting feature in our sample. Figure 7 illustrates the analysis conducted for B20 within our sample. The error associated with the DM value for this burst was 0.009 pc cm^{-3} (refer to Table 1), corresponding to a smear time of approximately $80 \mu\text{s}$ within CHIME band. To account for this effect, we measured the ACF of the time profile at 100 DM steps ranging from -0.009 to 0.009 pc cm^{-3} , centered around the optimal DM value ($348.781 \text{ pc cm}^{-3}$). The figure displays the outcome at the DM value that maximizes our ACF, which is characterized by the greatest separation between the second Lorentzian peak and the fit to the broader envelope. It is to be noted that this DM value does not correspond to the true DM of the burst. We cannot reliably ascertain whether the peak is due to

a microstructure or can be attributed to amplitude modulated noise, which will create stronger power on the one bin level. We redid the analysis at higher time resolution, and the burst was too weak to extract any reliable estimates. If real, detecting such features at 600 MHz opens the possibility of ultra-fast emission features in brighter detections from other sources in the CHIME band. The remaining bursts in our bright sample did not show any interesting features in their ACF.

4. Discussion

4.1. Burst Rate Evolution

Active repeaters have shown variations in their burst rates over time. The rate can change from less than one burst per hour to more than 100 bursts per hour, as was observed for FRB 20121102A by Li et al. (2021a) in their 60 hr of observations spanning 47 days at 1.2 GHz above a 7σ threshold of 0.015 Jy ms . Gajjar et al. (2018) also reported clustered arrival times in their high-frequency (4–8 GHz) study of the same source. Nimmo et al. (2023) also observed this behavior from FRB 20200120E, where they detected 53 bursts within 40 minutes, almost 80 bursts per hour. Before this epoch, the observed peak rate from the source was $0.4_{-0.4}^{+2.0}$ bursts per hour in their Effelsberg observations at 1.4 GHz above a 7σ threshold of 0.05 Jy ms . These burst storms after a dormant period can be a characteristic feature of some repeating sources. Notably, these observations were at different frequencies and sensitivity thresholds, making it harder to compare the rates and energy distributions among active repeaters.

CHIME/FRB, in its continuous monitoring, has been crucial in catching spontaneously active repeaters. FRB 20201124A is a prime example (Lanman et al. 2022). After its initial discovery in 2020 November, it was not detected above our sensitivity threshold (CHIME/FRB Collaboration et al. 2021) and suddenly entered a high-activity period in 2021 April. Follow-up observations led to detections of thousands of bursts using multiple instruments, particularly by the Five hundred meter Aperture Spherical Telescope (FAST; Xu et al. 2022). Recently, FRB 20220912A (Mckinven & CHIME/FRB Collaboration 2022) has shown similar behavior, with no bursts detected prior to 2022 September followed by nine bursts in three CHIME/FRB transits, suggesting rates as high as 200–300 bursts per day. Higher-frequency follow-ups by the Green Bank Telescope (GBT; Feng et al. 2023) and FAST (Zhang et al. 2023) confirmed this high burst rate for the source. Magnetars have also been known to exhibit burst storms at X-ray energies, with hundreds of bursts per hour (e.g., Gavriil et al. 2002; Younes et al. 2020). SGR 1935+2154 is a prime example, but so far, we have only observed one radio burst from this or any magnetar with a luminosity comparable to that of FRBs (CHIME/FRB Collaboration et al. 2020a; Bochenek et al. 2020).

We do not see any episodes of heightened activity from FRB 20180916B, even after ~ 200 hr of observation by CHIME/FRB across the entire activity phase. Cycle-to-cycle variation has been observed within the same activity phase from the source at other frequencies (Pastor-Marazuela et al. 2021; Bethapudi et al. 2023). However, in our long-term monitoring of the source, we find such variations to be consistent with being Poissonian in their distribution (see Section 3.4). As shown in Figure 3, the burst count can vary

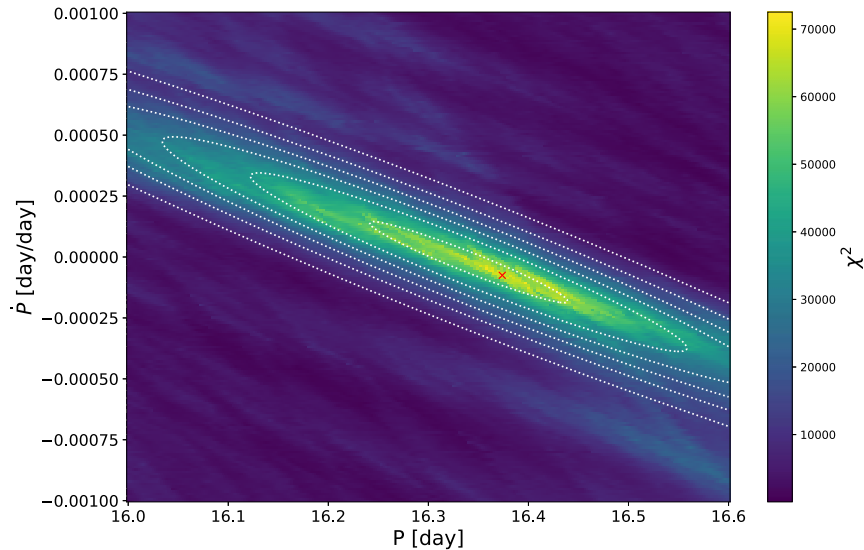


Figure 2. χ^2 distribution of different period (x-axis) and period derivative (y-axis) combinations. The red cross shows the maximum χ^2 value. The white contours show the results of the 2D Gaussian fit. We thus find $\dot{P} = -0.2 \pm 1.5 \times 10^{-4}$ day day $^{-1}$. We calculated the χ^2 using the Pearson χ^2 test described by CHIME/FRB Collaboration et al. (2020b). See Section 3.3 for details.

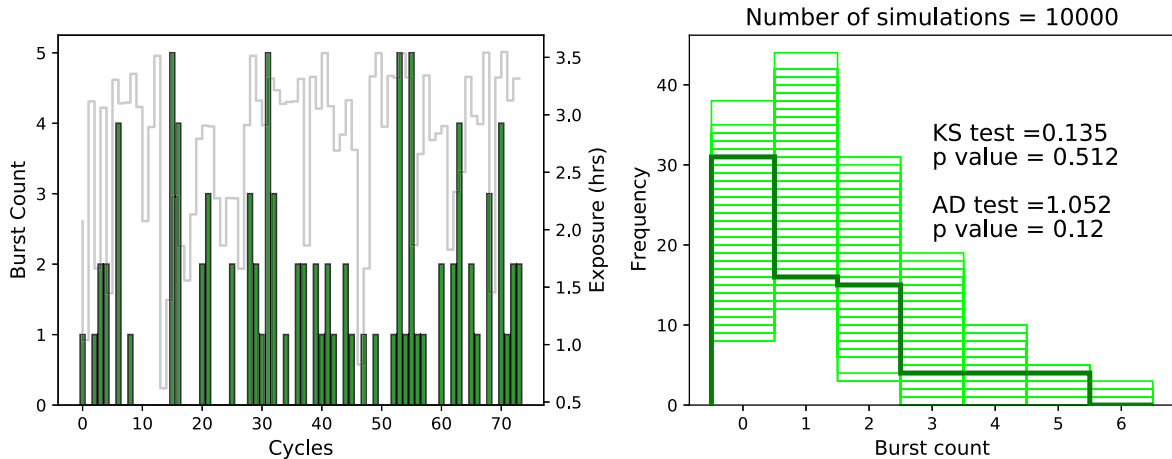


Figure 3. Distribution of burst counts for FRB 20180916B. The left panel shows the number of bursts detected during each activity cycle. One activity cycle is defined as a period of 16.34 days (starting 2018 August). The gray steps show the exposure in each cycle. In total, we have 74 activity cycles observed by CHIME/FRB from 2018 August to 2021 December. The right panel shows the frequency distribution of the burst count in each activity cycle in dark green. We also show a distribution from 10,000 simulations in light green sampled assuming a Poissonian process with mean rate equal to the value we have observed. We performed a K-S and A-D test between the observed and simulated distributions and report the median p -value, 0.512 and 0.12, respectively. See Section 3.4 for details.

from zero to five bursts from cycle to cycle, but such behavior is expected from a Poisson process of a mean rate of around 1.3 bursts per activity cycle. Figure 4 shows that the burst rate of the source is steady within 95% confidence uncertainty, assuming a Poissonian process in the observed 74 activity cycles. The source seems to have a steady rate, with no period of heightened activity, unlike what has been observed from other prolific repeaters. But the CHIME/FRB transit duration is ~ 15 minutes; extended exposure with a sensitive telescope might provide more insights into whether FRB 20180916B is prone to burst storms. In addition, the RM change observed in the source (Mckinven et al. 2023) does not coincide with any change in the activity of the source, suggesting that the secular rise observed likely has more to do with evolution in the propagation environment rather than variations in the intrinsic nature of the source.

FRB 20180916B is known to be chromatic in its activity. Higher-frequency bursts tend to be observed at earlier phases

(Pastor-Marazuela et al. 2021; Bethapudi et al. 2023) and lower frequency bursts tend to be observed at later phases (Pastor-Marazuela et al. 2021; Pleunis et al. 2021). This spectral dependence makes it difficult to estimate the full rate, across all frequencies, per cycle. In conjunction with the narrowband nature of the bursts, this can lead to differences in rates as a function of phase within a specific frequency range. In Figure 5, we see the overall rate of the source is consistent among activity phase within the uncertainties. With more detections in the future, any difference in rate might become prominent in the CHIME/FRB band.

Alongside rate, we find that the activity period of the source has not significantly varied with time since the source's discovery. Our estimate, based on data from 2018 August to 2021 December, the longest time span yet, is 16.34 ± 0.07 days (see Section 3.4), consistent with the original measurement of 16.35 ± 0.15 days (CHIME/FRB Collaboration et al. 2020b). This makes FRB 20180916B unique compared to other

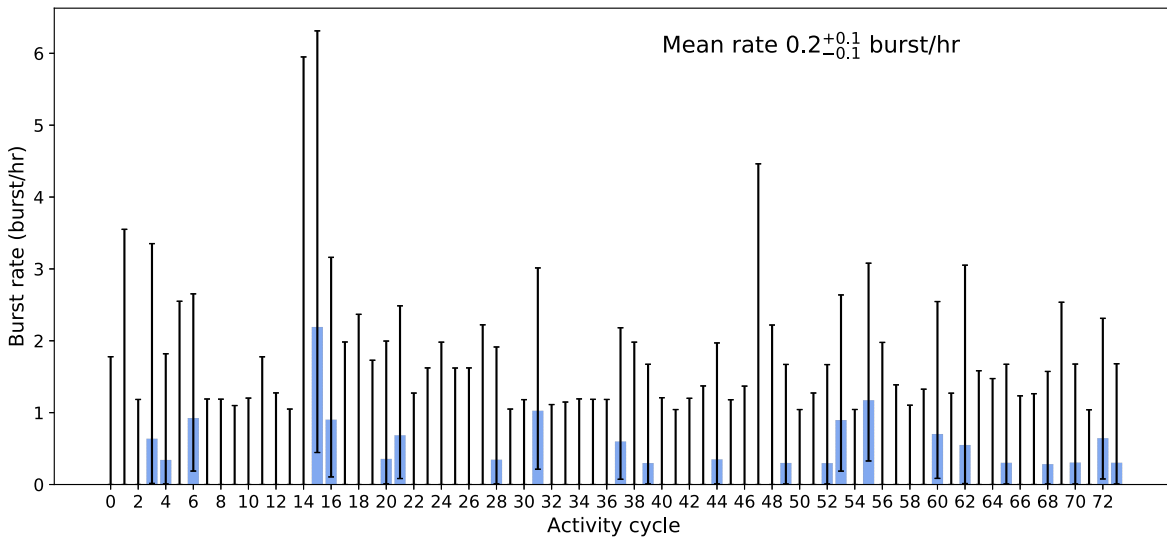


Figure 4. Burst rate in different activity cycles. The burst rate of FRB 20180916B (blue bars show detections) is steady within error bars, which denote 95% confidence intervals assuming a Poissonian process. Many of these cycles have zero rates where we denote upper limits. This is because not all of the bursts detected in our sample satisfy the exposure criteria (see Section 3.4 for details).

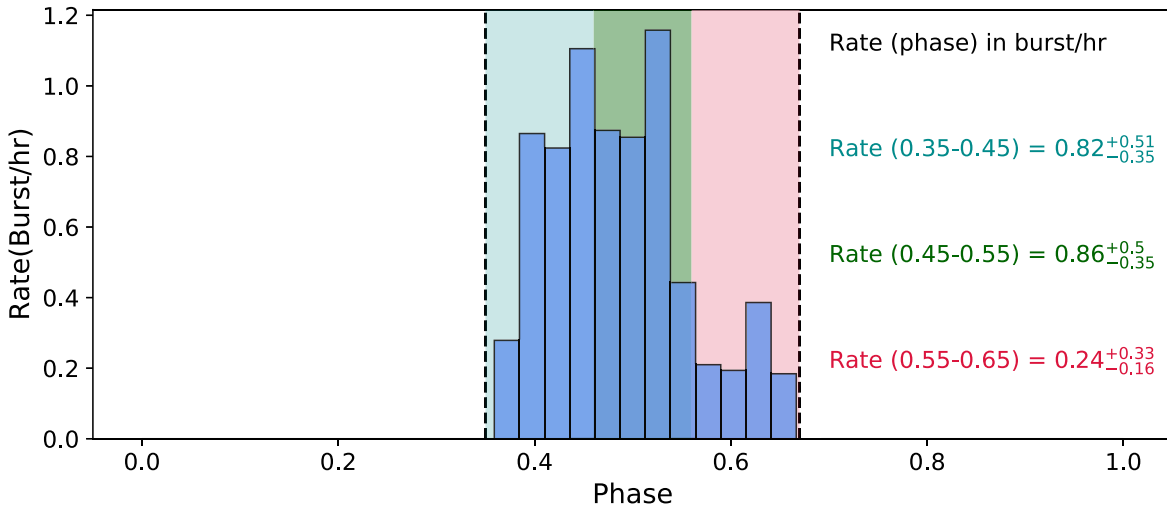


Figure 5. Burst rate variation with phase. We folded our burst arrival times at a period of 16.34 days with reference MJD 58369.40. We did the same with our calculated exposure and estimated the burst rate of FRB 20180916B in different phase bins. Here we have excised the bursts detected during days of low sensitivity and those detected outside the FWHM at 600 MHz to get true estimate on the rate. The rate is maximum in the phase range 0.45–0.55 (green). We also show the rates in phases earlier, i.e., 0.35–0.45 (blue) and later, i.e., 0.55–0.65 (red). The three rates are consistent within error bars (95%) assuming a Poissonian process. See Section 3.4 for details.

prominent repeaters. A stable period with no episodes of heightened activity might suggest a distinct progenitor scenario to what has been proposed for other active sources.

4.2. Spectro-temporal Properties

FRBs can have complex structures in their temporal profiles, often well described as multiple subbursts (J. Faber et al. 2023, in preparation). Repeaters generally show more such subbursts compared to apparent nonrepeaters, as was first noticed in the first known repeater FRB 20121102A (Hessels et al. 2019). Bursts from repeating sources also tend to be wider and have narrower bandwidths than for apparent one-off FRBs (Pleunis et al. 2021). Our burst sample from FRB 20180916B exhibits the same behavior. Most of our widths lie in the range 1–3 ms (see Table 1). Our bursts are wider than those seen in high-frequency detections at 6 GHz (~ 0.3 ms; Bethapudi et al. 2023)

and narrower compared to LOFAR detections (~ 40 ms; Pastor-Marazuela et al. 2021; Pleunis et al. 2021). Our average bandwidth of 150 MHz is narrower compared to bandwidth >500 MHz detections at high frequencies, a trend that has been seen for FRB 20180916B (Bethapudi et al. 2023) as well as FRB 20121102A (Gajjar et al. 2018; Hessels et al. 2019). We have observed subbursts as narrow as $78 \mu\text{s}$ (B20), suggesting there might be more submillisecond emissions from repeaters even at low frequencies. Additionally, as shown in Figure 6, we find no temporal or phase dependence in burst width over the 3 yr timescale. We also do not find any significant bimodality in the peak emitting frequency from the source, unlike what has been observed for FRB 20201124A (Lanman et al. 2022).

Scattering timescales trace inhomogeneities along the line of sight toward the source. FRB 20180916B’s low Galactic latitude ($b \sim 3.7^\circ$) implies a major contribution from the Milky Way ISM to the scattering time. The expected scattering in the

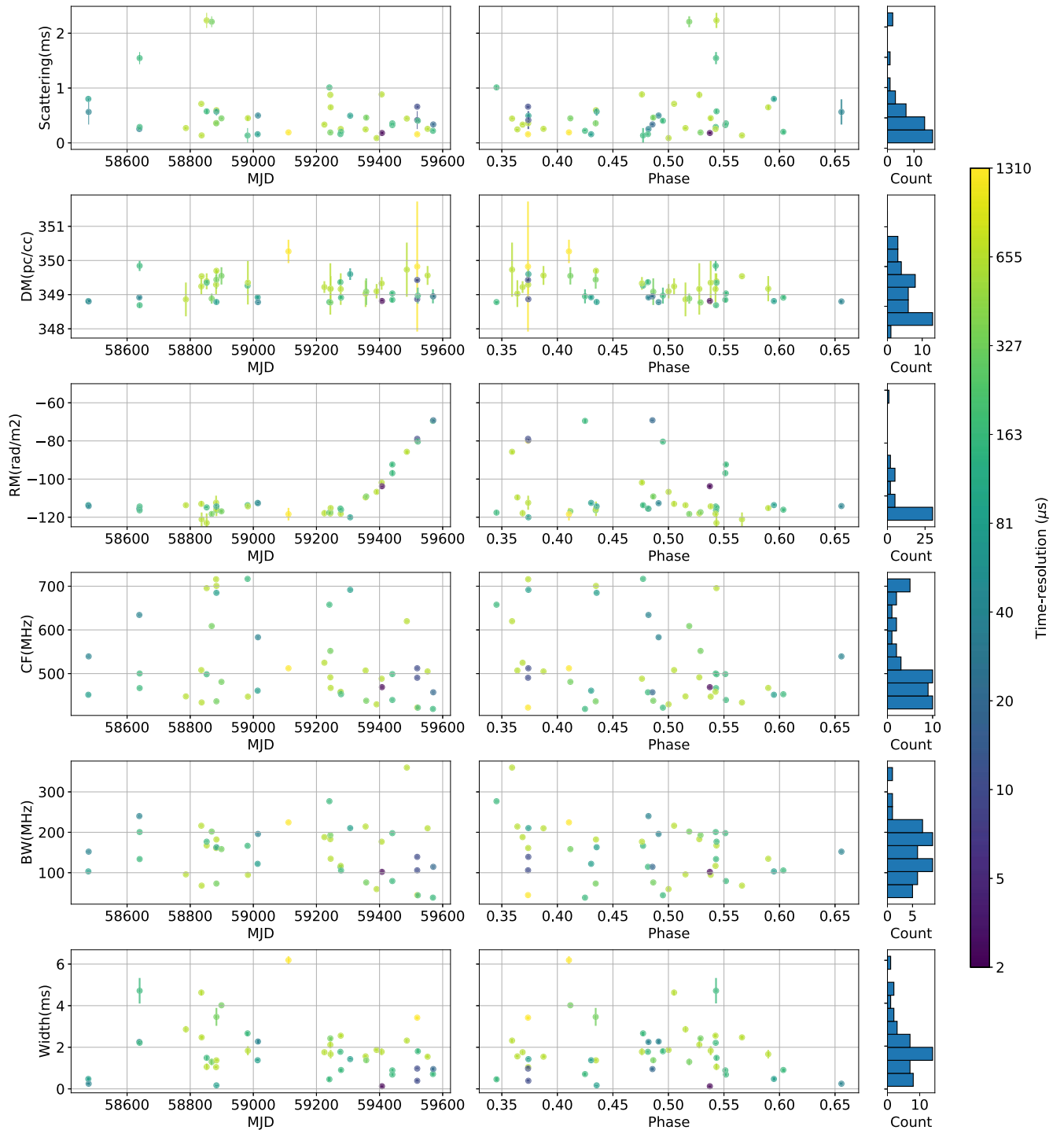


Figure 6. The evolution of various spectro-temporal properties of bursts from FRB 20180916B as a function of time (left) and phase of the 16.34 day cycle (reference MJD 58369.40). The histograms on the far right show overall distribution of the properties. We show here six properties: scattering, DM, RM, central frequency (CF), bandwidth (BW), and combined width of all of the subbursts (W). The color scale shows the time resolution at which we measured the morphological parameters for each of the burst since not all bursts were bright enough to be studied at $2.56 \mu\text{s}$ time resolution. We see the RM increase in the source around 2021 April as reported by McKinven et al. (2023). We find no trend in any other properties in both time and phase. Only the bursts with baseband data have been shown here since we were able to better characterize their spectral and temporal properties. (See Section 3.5 for details).

direction of FRB 20180916B at 600 MHz according to the NE2001 model (Cordes & Lazio 2002) for the Galactic electron distribution is ~ 0.16 ms. Assuming that the frequency dependence of scattering time is a power law with index -4 , we expect a scattering timescale of the order of ~ 0.17 ms in the CHIME band, extrapolating from the $2.7 \mu\text{s}$ scattering time reported by Marcote et al. (2020) at 1700 MHz using

scintillation bandwidth measurements. Chawla et al. (2020) reported an upper limit of 1.7 ms at 350 MHz, corresponding to a scattering timescale < 0.2 ms at 600 MHz. Our scattering values range from 0.08–2.2 ms, suggesting time variability in the medium causing the scattering. In our data set, we observed bursts with scattering less than 0.16 ms (see Table 1). However, our measured scattering might be contaminated by unresolved

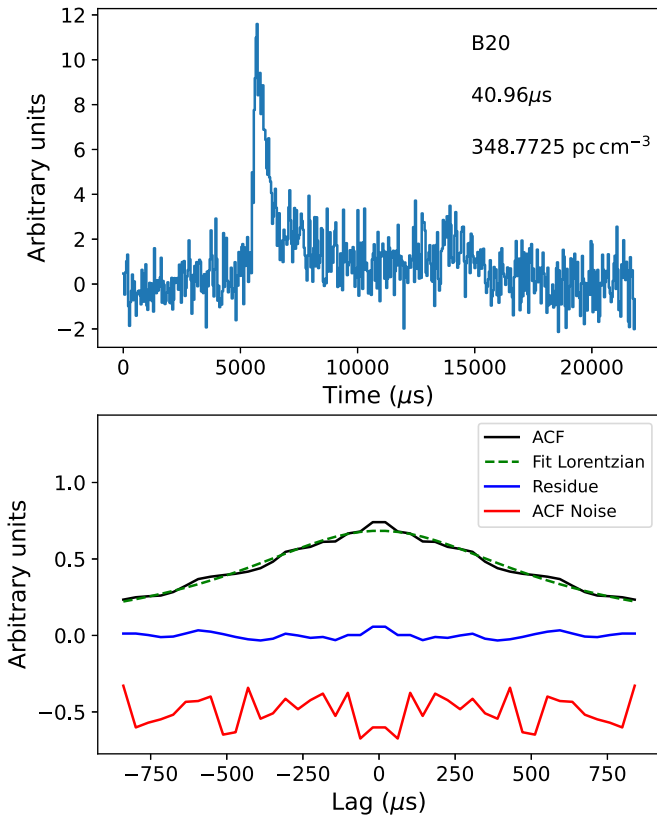


Figure 7. Microstructure analysis of B20 from FRB 20180916B. The top panel shows the burst profile, with the burst number, resolution at which it was extracted and the DM indicated in the top right. The bottom panel shows the temporal ACF (black), Lorentzian fit to the ACF (green dashed), the residual (blue), and ACF of the noise (red). We find a weak peak in the ACF with width of $\sim 50 \mu\text{s}$ but cannot constrain the true nature of this structure with the present data set. See Section 3.6 for details.

structure, since not all of the bursts in our sample are bright enough to be studied down to $2.56 \mu\text{s}$ (see Table 1). Most of the scattering observed from FRB 20180916B has been attributed to the Milky Way ISM (Marcote et al. 2020; Bethapudi et al. 2023; Sand et al. 2022) using scintillation bandwidth measurements. Hence, the observed scattering profile for the source, if real, may not always follow a power-law index of -4 , as expected from a thin screen model. Such deviations in the index have also been observed for Galactic pulsars (Lewandowski et al. 2015; Geyer et al. 2017). Bethapudi et al. (2023) also found tentative scattering variability from scintillation measurements; they attributed most of this to the refractive timescale of the Milky Way screen.

Microstructures have been observed for many FRB sources, suggesting luminous ultra-fast emission (Nimmo et al. 2022). For FRB 20180916B, we have seen structures as narrow as $3 \mu\text{s}$ at 1700 MHz (Nimmo et al. 2021) and $30 \mu\text{s}$ at 800 MHz (Sand et al. 2022), which is in agreement with the prediction of Milky Way scattering from NE2001. Although we did not find strong evidence for structure in this work, future studies should continue to search for short timescale structure from FRB 20180916B and other FRBs, especially those at higher galactic latitudes where Galactic scattering should be even smaller. Detecting such structures will suggest an occasionally less-turbulent environment that does not inhibit the propagation of microsecond substructures by scattering, even at low

frequencies. Microstructure also favors the emission origin to be magnetospheric instead of a shock wave interaction, since the latter’s larger physical scales do not naturally predict very short temporal behavior, whereas the former is inherently compact (Metzger et al. 2019; Lu et al. 2020).

4.3. Local Environment

Repeaters are a unique tool for understanding the immediate surroundings of FRBs, as they permit studies of short-term and long-term variability of DM, RM, and scattering properties. The first repeating source FRB 20121102A was proposed to be in a highly magnetized environment given its extremely high RM and association with a persistent radio source (Michilli et al. 2018). Since then, there has been a secular decrease in RM from the source with an increase in DM (Hilmarsson et al. 2021). This change can be explained by an FRB source within a magnetar wind nebula, a pulsar orbiting a supermassive black hole, or an evolving supernova remnant (SNR; Margalit & Metzger 2018; Zhang 2018). RM variability has also been observed for FRB 20201124A (Hilmarsson et al. 2021; Xu et al. 2022) on timescales of weeks. A more extreme case of this has been shown by FRB 20190520B, where a reversal in RM sign was observed (Anna-Thomas et al. 2023; Dai et al. 2022). Such variability can be attributed to variation in the magnetic field configuration close to the source region. Wang et al. (2022) suggested that these two sources might reside in a magnetar/Be binary star system, with interaction from the Be star decretion disk producing these RM variations.

FRB 20180916B has a nominal RM, which was reasonably stable with stochastic variations, until recently when Mckinven et al. (2023) observed a secular rise in the value. We do not see any corresponding evolution in the DM of the source. Mckinven et al. (2023) attributed this to changes in the B_{\parallel} of the local environment and put a limit of $\leq 4 \text{ pc}$ on the size of the Faraday active medium. This is greater than the 1 pc upper limit on the compact radio counterpart of FRB 20121102A (Plavin et al. 2022). Zhao et al. (2023) interpreted the RM variation of FRB 20180916B as periastron passage of a freely precessing magnetar in an orbital period of 1600–16,000 days with no DM contribution from stellar wind or disk. We do not see any changes in the scattering timescale that might hint at an interaction with a stellar wind during the RM variation epochs. However, the mass-loss rate of the companion star may be too low to discern any significant changes.

We find no obvious trend in the long-term variations in scattering, although burst-to-burst measurements tend to vary. Interestingly for bursts B4–B5 and B10–B11, we observe large fluctuations in the measured scattering value within the same transit. Ocker et al. (2023) also observed changes in scattering on short timescales (\sim minutes) for FRB 20190520B. They attribute such behavior to a dynamic, inhomogeneous plasma in the circumsource environment and predicted similar variations in other FRB sources. Though our measured values might not be physical scattering due to the possibility of underlying structures, we can put definitive limits at the given time resolution for respective bursts. Overall, this suggests that although FRB 20180916B has a cleaner circumburst medium compared to other sources, we can still expect considerable variations due to discrete plasma patches in the circumstellar medium (Ocker et al. 2023). Similar to us, Gopinath et al. (2023) also observed large scattering changes ($\sim 10 \text{ ms}$) on short timescales for FRB 20180916B in their observation at

150 MHz using the LOFAR telescope. They also attributed these to variations in the turbulence in the local environment. They did not find any phase dependence in scattering. We also do not observe any periodic dependence in scattering variability (see Figure 6). This seems at odds with strong binary wind interactions near the source if we assume that the 16 day periodicity is due to orbital motion. We also do not observe any correlation between changes in scattering with DM for FRB 20180916B, unlike what has been seen for the Crab pulsar over its long-term monitoring (McKee et al. 2018). These correlations have been attributed to seeing different sight lines through the nebula due to the pulsars proper motion, which traces the filamentary structure of the nebula. This suggests that FRB 20180916B might not reside in a Crab-like remnant, or may be older, with the remnant so dissipated that it has lost its filamentary structure.

4.4. Constraints on Progenitors

The periodic nature of FRB 20180916B has led to multiple progenitor theories. These can be broadly classified into two types. The first type involves FRB emission from a compact object, where the period is due to rotation, or to precession (either of an isolated object or of one in a binary system). The second broad class invokes a compact object in a binary orbit, where interactions with the companion wind or disk lead to FRB emission, and the orbital period explains the periodicity.

4.4.1. Rotation or Precession as the Origin of the Periodicity

The rotation of an ultra-long period magnetar has been suggested to explain the periodicity (Beniamini et al. 2020). In this case, an isolated magnetar is slowed down to a 16 day rotation period by episodic mass loss in particle winds, angular momentum kicks, or accretion due to a long-lasting fallback disk. The magnetar, in this case, would be of age comparable to that of typical Galactic magnetars (~ 1 – 10 kyr), which is consistent with the observed offset of the source from a star formation region in Hubble observations (Tendulkar et al. 2021). The stability of the period over the 3 yr of our observations is consistent with this scenario; however, the constancy of the burst rate is somewhat at odds with the usually more episodic magnetar bursting behavior. In this picture, we expect no phase-related DM variations and relatively constant polarization angles. However, we have not observed such long periods from any Galactic magnetars/neutron stars, though a possibility of a 6.7 hr period has been proposed for the unusual X-ray source 1E 161348–5055 in the SNR RCW 103 (De Luca et al. 2006).

Free precession in a flaring magnetar or luminous radio pulsar has also been suggested to explain the periodicity (Levin et al. 2020; Zanazzi & Lai 2020; Katz 2021). This model predicts an increase in the period as the neutron star spins down with time. Our upper limit, $\dot{P} < 1.5 \times 10^{-4}$, implies a lower limit on the spindown age $\gtrsim 150$ yr, or equivalently $B \gtrsim 5 \times 10^{14}$ G assuming standard magnetic braking (Levin et al. 2020; Katz 2021). These constraints will improve with time, although as noted by Katz (2021), the lower limit on the (unknown) spindown age is not constraining, since the latter is generally interpreted as an upper limit on the true age. Additionally, in such models, a shorter timescale periodicity from the rotation of the compact object itself is expected to be present, possibly on the order of seconds, as for Galactic

magnetars (e.g., Olausen & Kaspi 2014). This has not yet been seen, though detection could be hindered by timing noise or glitches in the case of a very young magnetar (e.g., Kaspi et al. 2000; Gavriil et al. 2008).

To explain the chromatic nature of the burst arrival times from FRB 20180916B, Li & Zanazzi (2021) suggested altitude-dependent emission from a magnetar, which can be precessing or have a long spin period. For a rotating magnetar, the model predicts a constant position angle at similar phases, but for a precessing system, the position angle can vary at fixed phase. In addition, the spindown rate could help distinguish between the two possibilities, since it is expected to be much larger in the case of free precession (Li & Zanazzi 2021).

Recently, Zhao et al. (2023) proposed a precessing magnetar in orbit with a Be star for FRB 20180916B, to explain its latest RM evolution. In this case, the 16.3 day period is due to a precessing or rotating magnetar, but it is in a binary orbit of ~ 1600 – $16,000$ days. In the model, the magnetar is undergoing a periastron passage, resulting in a secular rise in RM due to interaction with the disk of the Be star. Stochastic RM variations in this model are due to clumps in the stellar winds/disk interacting with the FRB. However, DM and scattering variations correlated with RM are expected in this model, yet our observations show no evidence for this.

Forced precession due to a fallback disk has also been proposed to explain the observed periodicity (Tong et al. 2020). Here, a shorter rotational periodicity from the compact object is also expected. This model does not obviously account for chromatic periodicity (Li & Zanazzi 2021), and a range of polarization position angle values is expected, but has not been observed (Nimmo et al. 2021; Mckinven et al. 2023). The forced precession fallback disk model is thus not favored by the data. The model predicts that the observed period should increase as the disk dissipates, such that $\dot{P} = -P/t_{\text{diss}}$, where t_{diss} is the unknown dissipation timescale (Katz 2021). Our constraint on \dot{P} implies $t_{\text{diss}} \gtrsim 300$ yr.

Another model involves geodetic precession in a relativistic orbit. Yang & Zou (2020) proposed a neutron star precessing in a tight orbit with a companion (orbital period ~ 100 – 1000 s). This system would be short-lived, and a decrease in the period and a change in burst rate would be expected as the orbit decays. However, the timescale of this decay could range from hundreds to millions of years (van Haften et al. 2012; Katz 2021), depending strongly on the distance between objects and their masses. Our current period derivative limit of 1.5×10^{-4} days day $^{-1}$ suggests that we will start probing interesting phase space (e.g., mass ratios of unity and a neutron star mass) in just a few years.

The last precessional model we consider here is a compact object in an ultraluminous X-ray binary undergoing super-Eddington mass transfer (Sridhar et al. 2021). Here, the precession of the polar accretion funnel results in periodic FRB emission. In this case, a systematic variation in DM of ~ 0.1 – 1 pc cm $^{-3}$ and an RM of ~ 0.5 – 1 rad m $^{-2}$ with activity phase is expected, depending on the parameters for the quiescent jet, taking into consideration the optical depth needed for FRB to escape. As shown in Figure 6, we constrain $\Delta\text{DM} \lesssim 1$ pc cm $^{-3}$ within the activity phase. However, this model does not naturally explain the observed evolution in RM if the variation is due to changes in the immediate emission environment. Moreover, a “turn-off” in emission is predicted

on a timescale of years, perhaps followed by the appearance of an optical/IR counterpart.

4.4.2. Binary Motion as Origin of Periodicity

The source of the radio bursts in FRB 20180916B has been suggested to be in different types of binary orbits in order to explain the observed 16.34 day periodicity.

Lyutikov et al. (2020) suggested a pulsar in orbit with an O/B type star, and Li et al. (2021b) suggested FRB emission from star quakes occurring due to stress on the neutron star surface by accreting material from a Be star companion. Ioka & Zhang (2020) proposed a highly magnetized pulsar whose magnetic field is “combed” by a strong wind from a massive companion star, resulting in FRB emission. Wada et al. (2021) made additional alterations to the model to explain the chromatic periodicity, by proposing variations in emitting frequency with phase due to the influx of aurora particles at different phases of the orbit. Deng et al. (2021) considered an accreting system with a compact object generating FRBs by the synchrotron maser mechanism. Wang et al. (2022) explained the RM variations observed in FRB 20201124A and FRB 20190520B using an eccentric magnetar/Be star binary model. Here, a Be star has a magnetized decretion disk, and when its binary companion magnetar approaches periastron, the radio waves interact with the disk, resulting in the observed RM variation.

Such models naturally predict DM and scattering time variations with phase, which we do not see. We can look to Galactic neutron star/OB binary systems for indications of the expected sizes of DM or scattering variations due to changes in location of the radio source within the companion wind. Johnston et al. (2001) studied the highly eccentric ($e = 0.87$) 3.4 yr radio pulsar/Be star binary PSR B1259–63, which exhibited DM variations of over $\sim 10 \text{ pc cm}^{-3}$, and scattering times that ranged from 0.1 to nearly 10 ms at 1.5 GHz, both correlated with orbital phase. Similarly, Andersen et al. (2023) studied the CHIME/FRB-discovered pulsar/OBe star binary PSR J2108+4516, which has an orbital period 269 days and eccentricity 0.09, showing that the pulsar exhibited DM variations of amplitude $\sim 4 \text{ pc cm}^{-3}$, and scattering times ranging from well under 1 ms to over 20 ms in the CHIME band, both also correlated with orbital phase. The latter system, with only modest eccentricity (0.09), has a projected semimajor axis of over 800 light seconds, implying only modest proximity of the two objects.

In FRB 20180916B, by contrast, we do not observe any such correlated DM or scattering variations, in spite of strong modulation of the burst rate. On the whole, this argues against a binary orbit with a massive star as the origin of the periodicity in FRB 20180916B’s burst rate.

We note that a massive companion with a weak wind might be invoked to explain the lack of scattering and DM variability. This has been observed for the pulsar binary PSR J0045–7319 in the Small Magellanic Cloud (SMC; Kaspi et al. 1996). Here the apparent low mass-loss rate of the companion, as implied by the absence of any DM variation in spite of a highly eccentric orbit and great proximity of the sources at periastron, is explained as a result of the low metallicity of the SMC, and the fact that OB stars have radiatively driven winds that make use of metals for the mass-loss mechanism. However, the host galaxy of FRB 20180916B has a metallicity similar to that of the Milky Way, which suggests that any binary companion to

FRB 20180916B would have a wind with Milky Way–type metal abundances (Marcote et al. 2020).

These models also predict a longer activity window at higher frequencies, which has not been observed and which also cannot easily explain the chromatic nature of the periodicity.

Finally, a neutron star in orbit with a magnetized white dwarf has been argued to produce FRB emission by accretion (Gu et al. 2020; Chen et al. 2022). This model requires a highly eccentric orbit to explain the duty cycle for FRB 20180916B. Dai & Zhong (2020) proposed an old, slowly spinning pulsar captured by a star interacting with an extragalactic asteroid belt. Here, interaction of asteroids with the magnetosphere of the neutron star leads to FRB emission. However, the recent dramatic long-term rise in RM is not naturally explained in this model.

Overall, the origin of the periodicity in FRB20180916B remains a mystery, with our observations providing key new constraints that further challenge existing models.

5. Conclusion

In this study, we report a morphological analysis of 60 bursts observed from the periodic FRB source FRB 20180916B, using data from CHIME/FRB from 2018 August to 2021 December. Out of these, 45 bursts were recorded with high-time-resolution baseband data, which enabled us to study their properties in detail. We present a comprehensive outline of our pulse morphology pipeline, which has been integrated into the baseband processing system, and employ it to measure the DM and spectro-temporal properties of the bursts in our data set.

Our analysis reveals that the variation in DM for FRB 20180916B is constrained to be $\lesssim 1 \text{ pc cm}^{-3}$, in agreement with findings from other telescopes operating at different wavelengths. Furthermore, we measured scattering times, and found evidence for variation from burst to burst, ranging from ~ 0.16 to over 2 ms, although in some cases unresolved microstructure may impact the measurement. We find no evidence for a correlation of scattering time with the phase of the 16 day cycle. The lack of phase-dependent DM or scattering times seems at odds with models for the periodicity involving a binary orbit around a massive star. Additionally, we found no correlation between any morphological property and the reported secular RM increase of the source (Mckinven et al. 2023). We also estimated the source activity period and provided constraints on the period derivative. Our analysis shows that the activity period of the source has remained unchanged, with a value of 16.34 ± 0.07 days, and the period derivative is constrained to be $-0.2 \pm 1.5 \times 10^{-4} \text{ day day}^{-1}$. The burst count of the source in each activity cycle was found to be consistent with a Poisson process, and the rate of the source showed no significant variation over our observation of 74 activity cycles. Unlike other prolific repeaters, FRB 20180916B appears stable in its emission and has not exhibited any heightened activity above our detection threshold. We also discussed and provided constraints on various isolated and binary models proposed to explain the periodic nature of the source. FRB 20180916B is an exciting puzzle, and further measurements of RM, DM, and scattering will hopefully provide insights into the evolution of the source environment and further constrain these models. Monitoring the source daily over an extended period will play a crucial role in this study, and CHIME/FRB is well positioned to undertake this task.

Acknowledgments

We thank the anonymous referee for providing comments that improved the manuscript.

CHIME is located on the traditional, ancestral, and unceded territory of the Syilx/Okanagan people.

We thank the Dominion Radio Astrophysical Observatory, operated by the National Research Council Canada, for gracious hospitality and expertise.

CHIME is funded by a grant from the Canada Foundation for Innovation (CFI) 2012 Leading Edge Fund (Project 31170) and by contributions from the provinces of British Columbia, Québec and Ontario. The CHIME/FRB Project is funded by a grant from the CFI 2015 Innovation Fund (project 33213) and by contributions from the provinces of British Columbia and Québec, and by the Dunlap Institute for Astronomy and Astrophysics at the University of Toronto. Additional support was provided by the Canadian Institute for Advanced Research (CIFAR), McGill University and the Trottier Space Institute via the Trottier Family Foundation, and the University of British Columbia. The CHIME/FRB baseband system was funded in part by a CFI John R. Evans Leaders Fund grant to I.H.S. The Dunlap Institute is funded through an endowment established by the David Dunlap family and the University of Toronto. Research at Perimeter Institute is supported by the Government of Canada through Industry Canada and by the Province of Ontario through the Ministry of Research & Innovation. The National Radio Astronomy Observatory is a facility of the National Science Foundation (NSF) operated under cooperative agreement by Associated Universities, Inc. FRB research at UBC is supported by an NSERC Discovery Grant and by the Canadian Institute for Advanced Research.

K.R.S. acknowledges support from Murata Family Fellowship and Fonds de Recherche du Québec—Nature et Technologies (FRQNT) Doctoral Research Award. V.M.K. holds the Lorne Trottier Chair in Astrophysics and Cosmology, a Distinguished James McGill Professorship, and receives support from an NSERC Discovery grant (RGPIN 228738-13), from an R. Howard Webster Foundation Fellowship from

CIFAR, and from the FRQNT CRAQ. K.N. is a Kavli Fellow. Z.P. is a Dunlap Fellow. K.S. is supported by the NSF Graduate Research Fellowship Program. B.C.A. is supported by an FRQNT Doctoral Research Award. M.B. is a McWilliams fellow and an IAU Gruber fellow. A.M.C. is funded by an NSERC Doctoral Postgraduate Scholarship. A.P. C. is a Vanier Canada Graduate Scholar. F.A.D is supported by the UBC Four Year Fellowship. G.E. is supported by an NSERC Discovery grant (RGPIN-2020-04554) and by a Canadian Statistical Sciences Institute (CANSSI) Collaborative Research Team Grant. B.M.G. is supported by an NSERC Discovery grant (RGPIN-2022-03163), and by the Canada Research Chairs (CRC) program. K.W.M. holds the Adam J. Burgasser Chair in Astrophysics and is supported by NSF grant Nos. 2008031 and 2018490. A.P. is funded by the NSERC Canada Graduate Scholarships—Doctoral program. A.B.P. is a Banting Fellow, a McGill Space Institute (MSI) Fellow, and an FRQNT postdoctoral fellow. D.C.S. is supported by an NSERC Discovery grant (RGPIN-2021-03985) and by a Canadian Statistical Sciences Institute (CANSSI) Collaborative Research Team Grant.

Facility: CHIME.

Software: *astropy* (Astropy Collaboration et al. 2013, 2018, 2022), *bitshuffle* (Masui 2017), *DM_Phase* (Seymour et al. 2019), *emcee* (Foreman-Mackey et al. 2013), *HEALPix* (Górski et al. 2005), *healpy* (Zonca et al. 2019), *hdf5* (The HDF Group 1997–2023), *matplotlib* (Hunter 2007), *numpy* (Harris et al. 2020), *pandas* (The pandas development team 2020), *scipy* (Virtanen et al. 2020), *statsmodel* (Seabold & Perktold 2010).

Appendix

Figures 8 and 9 show our burst sample with baseband data, with Table 1 listing their measured properties. Figure 10 shows the new detections with only intensity data, with measured morphological properties listed in Table 2.

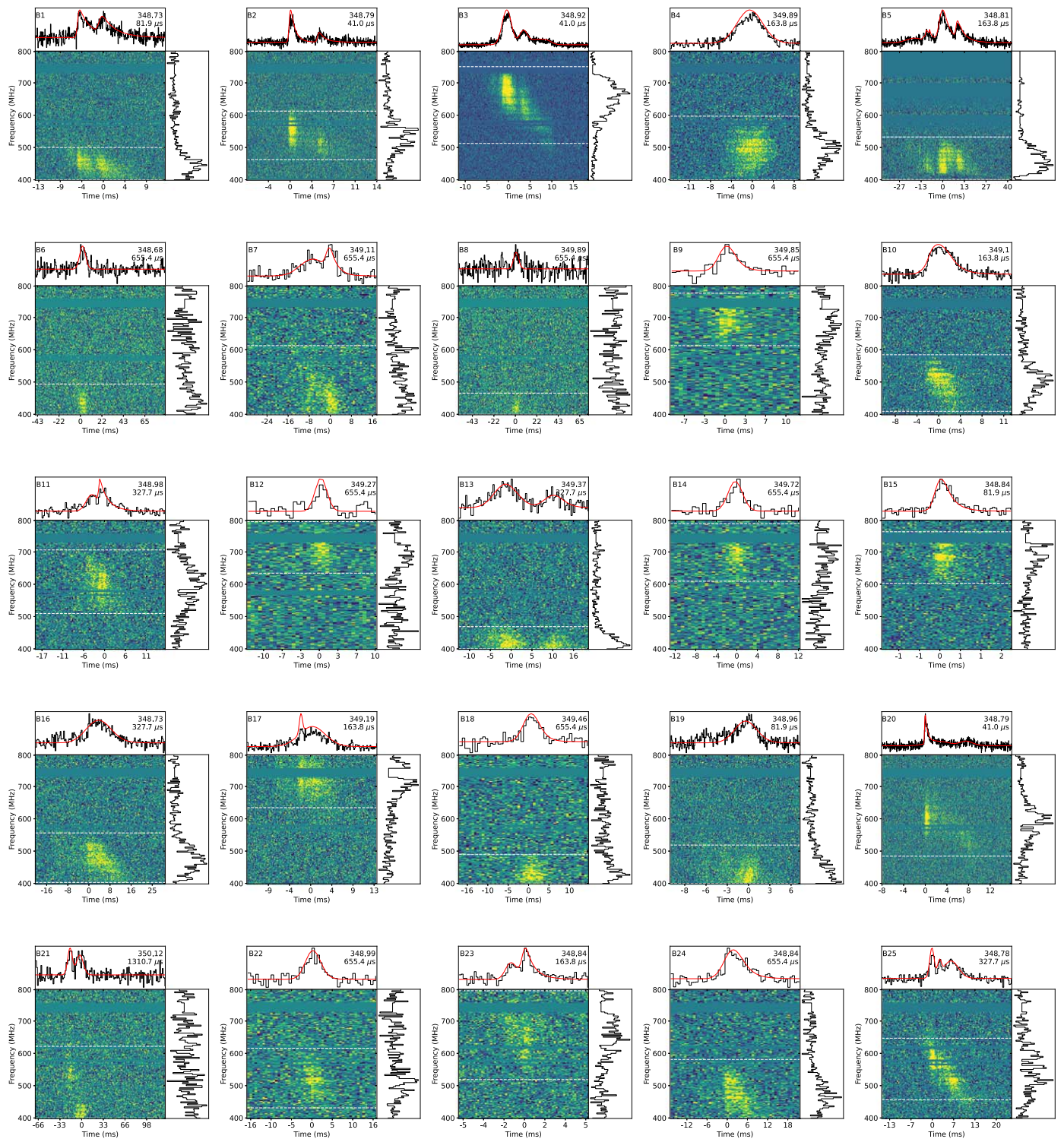


Figure 8. Figure showing bursts detected by the baseband system from FRB 20180916B dedispersed at their structure-maximizing DM. In each subfigure, the top panel shows the time series, with red line showing the best fit, the panel below it shows the dynamic spectra, and finally to the right of it is the frequency distribution of the power. The white-dotted lines show the extent of bandwidth. In the top right, we see the DM that it has been dedispersed to and the time resolutions to which it has been plotted in microseconds, and the top left shows the burst number. The number of channels here is 128. Intensity data waterfalls of bursts B1–B15 and B16–B21 have already been published in CHIME/FRB Collaboration et al. (2020b) and Pleunis et al. (2021), respectively.

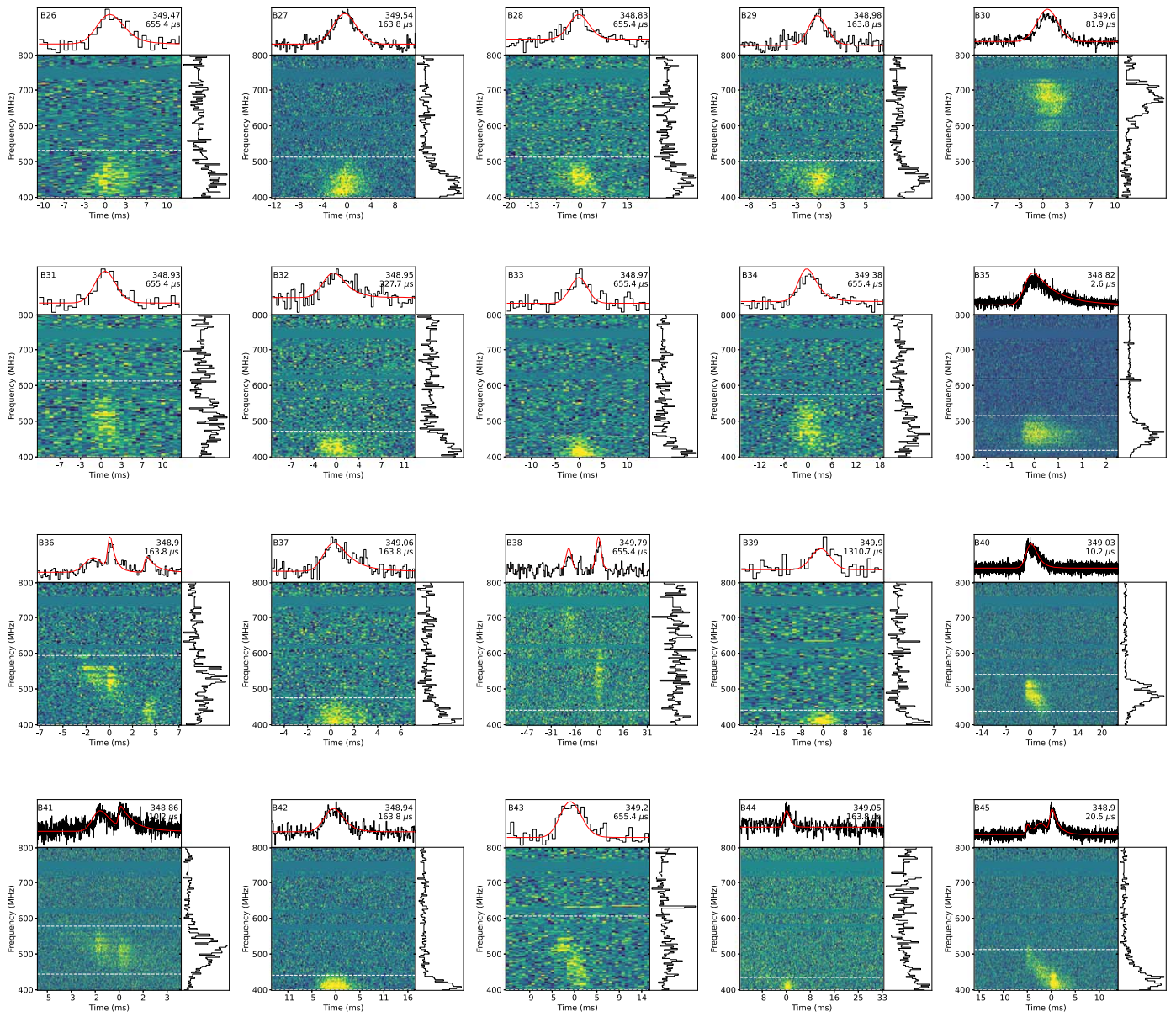


Figure 9. Continued from Figure 8.

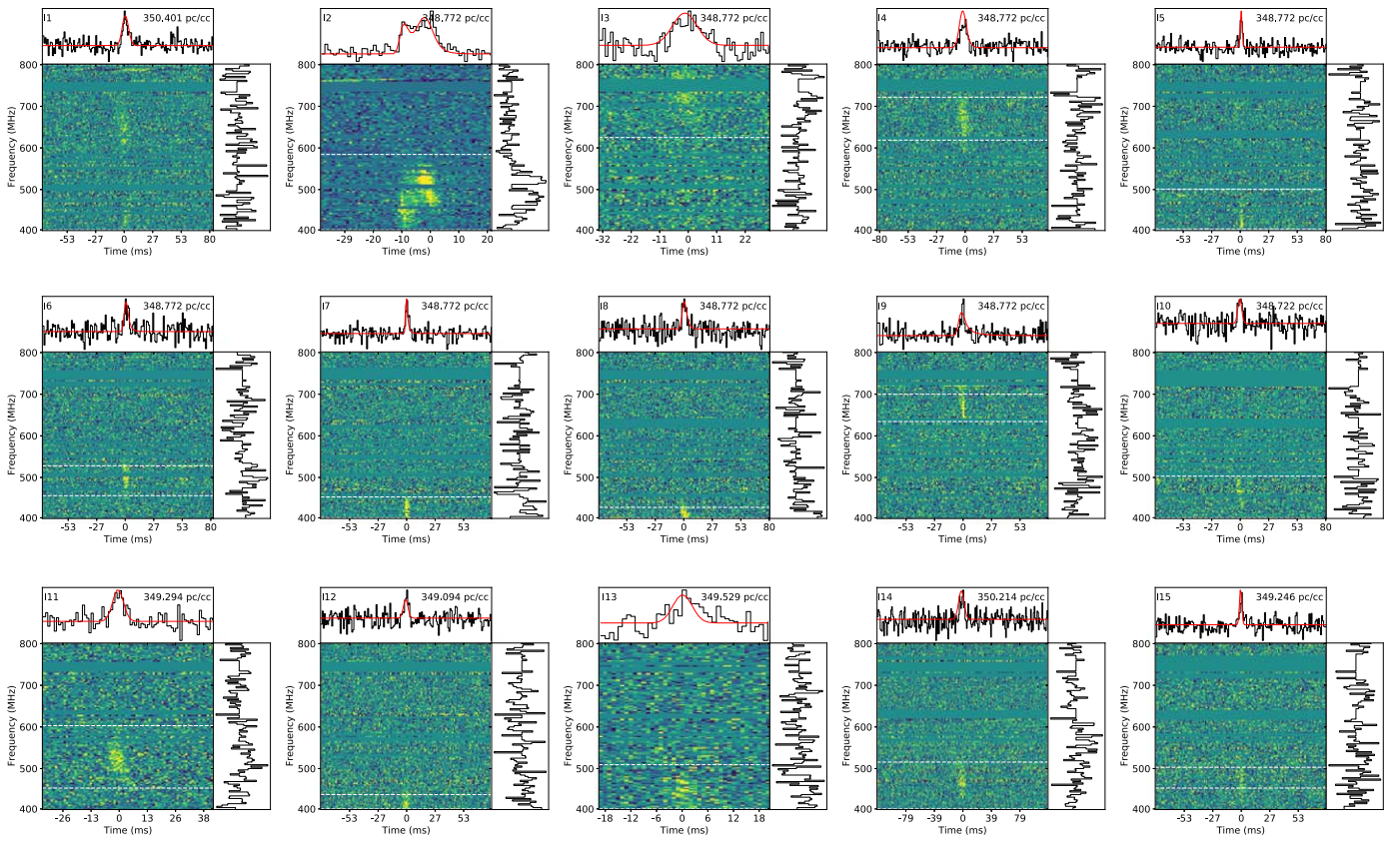


Figure 10. Waterfall figure similar to Figure 8 showing bursts detected from FRB 20180916B only with intensity data from 2020 September 20 until 2021 December 31. All of these bursts are shown at a resolution of 0.983 ms and 128 channels.

Table 1
Table Showing the Morphological Properties of All of the Bursts Detected by the Baseband System

Burst	TNS	TOA (MJD)	P	D	DM (pc cm^{-3})	τ (ms)	σ (ms)	$\Delta\nu$ (MHz)
B1	20181225A	58477.161851	0.595	32	348.812(20)	0.802(22)	0.198(24) 0.434(59)	400.0–503.2
B2	20181226A	58478.15521	0.656	16	348.801(28)	0.564(230)	0.165(8) 0.186(25)	463.3–615.4
B3	20190604B	58638.716433	0.482	16	348.919(32)	0.253(1)	1.044(41) 0.873(3) 1.496(41) 0.996(66)	514.2–754.3
B4	20190605A	58639.705612	0.543	64	349.845(152)	0.290(3)	2.214(5)	400.0–600.6
B5	20190605B	58639.710081	0.543	64	348.690(83)	1.546(111)	4.396(577) 0.262(83) 1.568(54) 0.612(60)	400.0–533.7
B6	20191030B	58786.320749	0.515	256	348.861(494)	0.270(13)	2.863(156)	400.0–495.8
B7	20191218A	58835.173236	0.505	256	349.243(235)	0.712(6)	4.538(16) 0.924(141)	400.0–616.2
B8	20191219A	58836.171977	0.566	256	349.540(10)	0.137(3)	2.476(59)	400.0–468.0
B9	20200104E	58852.136284	0.543	256	349.390(234)	2.233(138)	1.058(162)	611.9–779.3
B10	20200104D	58852.137732	0.543	64	349.350(84)	0.575(38)	0.586(101) 1.372(82)	410.2–586.9
B11	20200120A	58868.075857	0.519	128	348.883(146)	2.209(99)	1.295(159) 0.105(37)	507.9–709.7
B12	20200203A	58882.046806	0.374	256	349.292(276)	0.360(6)	1.045(8)	635.4–796.5
B13	20200204B	58883.03995	0.435	128	349.438(264)	0.358(55)	2.718(215) 2.143(372)	400.0–473.1
B14	20200204D	58883.044053	0.435	256	349.699(56)	0.596(10)	1.372(22)	609.6–791.8

Table 1
(Continued)

Burst	TNS	TOA (MJD)	P	D	DM (pc cm^{-3})	τ (ms)	σ (ms)	$\Delta\nu$ (MHz)
B15	20200204E	58883.05372	0.435	32	348.785(67)	0.570(73)	0.169(18)	603.3–766.4
B16	20200220A	58899.007059	0.412	128	349.549(253)	0.448(4)	4.019(15)	402.0–560.3
B17	20200512A	58981.776623	0.477	64	349.264(85)	0.135(135)	0.306(3)	633.4–800.0
B18	20200513A	58982.771575	0.538	256	349.350(638)	0.451(34)	1.834(217)	400.0–494.6
B19	20200613A	59013.692871	0.43	32	348.923(36)	0.158(8)	1.376(34)	400.0–522.0
B20	20200614A	59014.685325	0.491	16	348.781(9)	0.499(3)	0.078(5)	485.2–681.1
B21	20200919B	59111.40643	0.41	512	350.265(342)	0.191(3)	2.014(6)	400.0–624.4
B22	20210111E	59225.104279	0.369	256	349.222(172)	0.333(12)	1.058(85)	430.9–619.0
B23	20210127E	59241.060714	0.345	64	348.783(33)	1.011(46)	5.115(30)	519.3–796.1
B24	20210130I	59244.043996	0.528	256	349.17(75)	0.876(60)	0.417(80)	400.0–583.0
B25	20210130H	59244.062294	0.529	128	348.772(3)	0.190(2)	0.193(48)	455.5–648.3
B26	20210131A	59245.058327	0.59	256	349.175(369)	0.649(48)	0.672(32)	400.0–534.5
B27	20210302A	59275.968773	0.482	64	349.366(54)	0.160(3)	2.268(4)	400.0–514.6
B28	20210303B	59276.96257	0.542	256	349.163(462)	0.254(8)	1.669(206)	400.0–516.9
B29	20210304A	59277.960337	0.603	64	348.913(43)	0.201(22)	1.783(14)	400.0–505.6
B30	20210402B	59306.8901	0.374	32	349.600(170)	0.495(2)	0.908(70)	586.5–796.9
B31	20210521C	59355.747585	0.364	256	349.030(392)	0.246(11)	1.430(5)	400.0–614.3
B32	20210523A	59357.746804	0.486	128	349.087(390)	0.461(32)	1.564(18)	400.0–475.9
B33	20210625A	59390.652027	0.5	256	349.100(211)	0.088(1)	1.378(135)	400.0–459.4
B34	20210711A	59406.600248	0.476	256	349.330(186)	0.884(55)	1.872(3)	400.0–576.7
B35	20210712A	59407.599363	0.537	1	348.814(11)	0.180(8)	1.784(172)	418.0–520.0
B36	20210814C	59440.507259	0.551	64	348.849(52)	0.324(21)	0.126(3)	400.0–597.8
B37	20210814B	59440.515848	0.552	64	349.035(36)	0.356(16)	0.868(75)	400.0–479.4
B38	20210929C	59486.389633	0.359	256	349.731(793)	0.443(4)	0.108(31)	439.9–800.0
B39	20211101D	59519.304104	0.374	512	349.823(1.9)	0.157(5)	1.514(95)	400.0–444.6
B40	20211101C	59519.304697	0.374	4	349.429(28)	0.660(9)	3.423(43)	437.5–543.5
B41	20211101B	59519.309086	0.374	4	348.867(19)	0.415(164)	0.976(12)	442.6–581.8
B42	20211103B	59521.288708	0.495	64	348.971(234)	0.403(29)	0.378(17)	400.0–444.2
B43	20211204D	59552.211828	0.388	256	349.562(276)	0.256(11)	0.087(11)	400.0–610.0
B44	20211221A	59569.162656	0.425	64	348.951(206)	0.220(14)	1.808(86)	400.0–438.3
B45	20211222B	59570.154978	0.486	8	348.950(32)	0.336(8)	0.711(72)	400.0–514.6
							0.239(20)	
							0.858(36)	
							0.334(11)	

Notes. The first column shows the burst number. Then we present their TNS names. Topocentric TOAs are in Modified Julian Date (MJD) format, referenced at 400 MHz with ~ 1 s precision. P corresponds to the phase of the burst folded at 16.34 days with reference MJD 58369.40. D is the downsampling factor at which we measured the properties (i.e., time resolution = $D \times 2.56 \mu\text{s}$). DM is the dispersion measure reported by `fitburst`. τ is the scattering timescale referenced at 600 MHz. σ is the intrinsic widths of all of the subbursts at 600 MHz. $\Delta\nu$ corresponds to the bandwidth of the detection. See Section 3.1 for details. Intensity data analysis of B1–B15 and B16–B21 has already been published in CHIME/FRB Collaboration et al. (2020b) and Pleunis et al. (2021), respectively. The rest are new detections.

Table 2
Morphological Properties of All of the Bursts Detected with Only Total Intensity Data Since the Last Published Data Set in Pleunis et al. (2021)

Burst	TNS	TOA (MJD)	P	DM (pc cm ⁻³)	τ (ms)	σ (ms)	$\Delta\nu$ (MHz)
I1	20201023B	59145.325356	0.515	350.401(23)	<5.287	2.644(298)	400.2–800.0
I2	20201123D	59176.244474	0.409	348.772(0)	0.943(109)	0.833(188), 2.233(198)	400.2–581.2
I3	20210129C	59243.059205	0.5	348.772(0)	<9.284	4.642(602)	501.1–800.0
I4	20210214D	59259.00883	0.477	348.772(0)	2.662(7)	1.779(8)	616.1–720.0
I5	20210301B	59274.9735	0.455	348.772(0)	2.303(617)	1.832(338)	400.0–499.0
I6	20210302G	59275.978095	0.516	348.772(0)	2.092(658)	1.603(260)	453.1–526.8
I7	20210320A	59293.904126	0.614	348.772(0)	2.080(477)	0.574(143)	419.4–449.1
I8	20210626A	59391.661298	0.6	348.772(0)	2.173(876)	1.364(268)	400.0–424.5
I9	20210711B	59406.606126	0.515	348.772(0)	0.562(3)	0.364(5)	631.8–699.2
I10	20210713C	59408.592801	0.637	348.722(32)	<3.155	1.577(303)	400.2–500.2
I11	183057477	59455.466284	0.507	349.294(23)	<4.463	2.232(244)	450.2–602.0
I12	20210930E	59487.382143	0.462	349.095(292)	<4.653	2.327(406)	400.2–435.4
I13	20210930D	59487.397668	0.463	349.530(55)	<4.349	2.174(278)	400.2–506.4
I14	20211118B	59536.265914	0.455	350.215(47)	<7.370	3.685(375)	400.2–512.2
I15	201096712	59553.209720	0.493	349.246(16)	<2.000	1.000(186)	450.2–500.2

Notes. The first column shows the burst number. We then present their transient name server (TNS) names. Topocentric TOAs provided here are in Modified Julian Date (MJD) format, referenced at 400 MHz. P corresponds to the phase of the burst folded at 16.34 days with reference MJD 58369.40. DM is the dispersion measure reported by `fitburst`. τ is the scattering timescale referenced at 600 MHz. σ is the intrinsic widths of all of the subbursts at 600 MHz. $\Delta\nu$ corresponds to the bandwidth of the detection. Some burst were too weak to get a reliable DM estimated; hence, we fixed their DM value to 347.772 pc cm⁻³ (Nimmo et al. 2021) and extracted their best-fit results.

ORCID iDs

Ketan R. Sand <https://orcid.org/0000-0003-3154-3676>
 Daniela Breitman <https://orcid.org/0000-0002-2349-3341>
 Daniele Michilli <https://orcid.org/0000-0002-2551-7554>
 Victoria M. Kaspi <https://orcid.org/0000-0001-9345-0307>
 Pragya Chawla <https://orcid.org/0000-0002-3426-7606>
 Emmanuel Fonseca <https://orcid.org/0000-0001-8384-5049>
 Ryan Mckinven <https://orcid.org/0000-0001-7348-6900>
 Kenzie Nimmo <https://orcid.org/0000-0003-0510-0740>
 Ziggy Pleunis <https://orcid.org/0000-0002-4795-697X>
 Kaitlyn Shin <https://orcid.org/0000-0002-6823-2073>
 Bridget C. Andersen <https://orcid.org/0000-0001-5908-3152>
 Mohit Bhardwaj <https://orcid.org/0000-0002-3615-3514>
 P. J. Boyle <https://orcid.org/0000-0001-8537-9299>
 Charanjot Brar <https://orcid.org/0000-0002-1800-8233>
 Tomas Cassanelli <https://orcid.org/0000-0003-2047-5276>
 Amanda M. Cook <https://orcid.org/0000-0001-6422-8125>
 Alice P. Curtin <https://orcid.org/0000-0002-8376-1563>
 Fengqiu Adam Dong <https://orcid.org/0000-0003-4098-5222>
 Gwendolyn M. Eadie <https://orcid.org/0000-0003-3734-8177>
 B. M. Gaensler <https://orcid.org/0000-0002-3382-9558>
 Jane Kaczmarek <https://orcid.org/0000-0003-4810-7803>
 Adam Lanman <https://orcid.org/0000-0003-2116-3573>
 Calvin Leung <https://orcid.org/0000-0002-4209-7408>
 Kiyoshi W. Masui <https://orcid.org/0000-0002-4279-6946>
 Mubdi Rahman <https://orcid.org/0000-0003-1842-6096>
 Ayush Pandhi <https://orcid.org/0000-0002-8897-1973>
 Aaron B. Pearlman <https://orcid.org/0000-0002-8912-0732>
 Emily Petroff <https://orcid.org/0000-0002-9822-8008>
 Masoud Rafiei-Ravandi <https://orcid.org/0000-0001-7694-6650>
 Paul Scholz <https://orcid.org/0000-0002-7374-7119>
 Vishwangi Shah <https://orcid.org/0000-0002-4823-1946>

Kendrick Smith <https://orcid.org/0000-0002-2088-3125>
 Ingrid Stairs <https://orcid.org/0000-0001-9784-8670>
 David C. Stenning <https://orcid.org/0000-0002-9761-4353>

References

- Amiri, M., Bandura, K., Chen, T., et al. 2023, *ApJ*, 947, 16
 Astropy Collaboration, Price-Whelan, A. M., Lim, P. L., et al. 2022, *ApJ*, 935, 167
 Astropy Collaboration, Price-Whelan, A. M., Sipőcz, B. M., et al. 2018, *AJ*, 156, 123
 Astropy Collaboration, Robitaille, T. P., Tollerud, E. J., et al. 2013, *A&A*, 558, A33
 Andersen, B. C., Fonseca, E., McKee, J. W., et al. 2023, *ApJ*, 943, 57
 Anna-Thomas, R., Connor, L., Burke-Spolaor, S., et al. 2023, *Sci*, 380, 599
 Bailes, M. 2022, *Sci*, 378, abj3043
 Beniamini, P., Wadiasingh, Z., & Metzger, B. D. 2020, *MNRAS*, 496, 3390
 Bethapudi, S., Spitler, L. G., Main, R. A., Li, D. Z., & Wharton, R. S. 2023, *MNRAS*, 524, 3303
 Bochenek, C. D., Ravi, V., Belov, K. V., et al. 2020, *Natur*, 587, 59
 Chawla, P., Andersen, B., Bhardwaj, M., et al. 2020, *ApJL*, 896, L41
 Chawla, P., Kaspi, V. M., Ransom, S. M., et al. 2022, *ApJ*, 927, 35
 Chen, H.-Y., Gu, W.-M., Fu, J.-B., et al. 2022, *ApJ*, 937, 9
 CHIME/FRB Collaboration, Amiri, M., Andersen, B. C., et al. 2021, *ApJS*, 257, 59
 CHIME/FRB Collaboration, Amiri, M., Andersen, B., et al. 2020b, *Natur*, 582, 351
 CHIME/FRB Collaboration, Amiri, M., Bandura, K., et al. 2018, *ApJ*, 863, 48
 CHIME Collaboration, Amiri, M., Bandura, K., et al. 2022, *ApJS*, 261, 29
 CHIME/FRB Collaboration, Andersen, B., Bandura, K., et al. 2020a, *Natur*, 587, 54
 CHIME/FRB Collaboration, Andersen, B. C., Bandura, K., et al. 2019, *ApJL*, 885, L24
 CHIME/FRB Collaboration, Andersen, B. C., Bandura, K., et al. 2023, *ApJ*, 947, 83
 Cordes, J. M., & Chatterjee, S. 2019, *ARA&A*, 57, 417
 Cordes, J. M., & Lazio, T. J. W. 2002, arXiv:astro-ph/0207156
 Cordes, J. M., Wharton, R. S., Spitler, L. G., Chatterjee, S., & Wasserman, I. 2016, arXiv:1605.05890
 Cruces, M., Spitler, L. G., Scholz, P., et al. 2021, *MNRAS*, 500, 448
 Dai, S., Feng, Y., Yang, Y. P., et al. 2022, arXiv:2203.08151
 Dai, Z. G., & Zhong, S. Q. 2020, *ApJL*, 895, L1

- De Luca, A., Caraveo, P. A., Mereghetti, S., Tiengo, A., & Bignami, G. F. 2006, *Sci*, **313**, 814
- Deng, C.-M., Zhong, S.-Q., & Dai, Z.-G. 2021, *ApJ*, **922**, 98
- Dickey, D. A., & Fuller, W. A. 1979, *JASA*, **74**, 427
- Feng, Y., Li, D., Zhang, Y.-K., et al. 2023, arXiv:2304.14671
- Fonseca, E., Andersen, B., Bhardwaj, M., et al. 2020, *ApJL*, **891**, L6
- Foreman-Mackey, D., Hogg, D. W., Lang, D., & Goodman, J. 2013, *PASP*, **125**, 306
- Gajjar, V., Siemion, A. P. V., Price, D. C., et al. 2018, *ApJ*, **863**, 2
- Gavriil, F. P., Gonzalez, M. E., Gotthelf, E. V., et al. 2008, *Sci*, **319**, 1802
- Gavriil, F. P., Kaspi, V. M., & Woods, P. M. 2002, *Natur*, **419**, 142
- Geyer, M., Karastergiou, A., Kondratiev, V. I., et al. 2017, *MNRAS*, **470**, 2659
- Gopinath, A., Bassa, C. G., Pleunis, Z., et al. 2023, arXiv:2305.06393
- Górski, K. M., Hivon, E., Banday, A. J., et al. 2005, *ApJ*, **622**, 759
- Gu, W.-M., Yi, T., & Liu, T. 2020, *MNRAS*, **497**, 1543
- Harris, C. R., Millman, K. J., van der Walt, S. J., et al. 2020, *Natur*, **585**, 357
- Hessels, J. W. T., Spitler, L. G., Seymour, A. D., et al. 2019, *ApJL*, **876**, L23
- Hilmarsson, G., Michilli, D., Spitler, L., et al. 2021, *ApJL*, **908**, L10
- Hilmarsson, G. H., Spitler, L. G., Main, R. A., & Li, D. Z. 2021, *MNRAS*, **508**, 5354
- Hunter, J. D. 2007, *CSE*, **9**, 90
- Ioka, K., & Zhang, B. 2020, *ApJL*, **893**, L26
- Johnston, S., Wex, N., Nicastro, L., Manchester, R. N., & Lyne, A. G. 2001, *MNRAS*, **326**, 643
- Joseph, A., Chawla, P., Fonseca, E., et al. 2019, *ApJL*, **882**, L18
- Kaspi, V. M., Lackey, J. R., & Chakrabarty, D. 2000, *ApJL*, **537**, L31
- Kaspi, V. M., Tauris, T. M., & Manchester, R. N. 1996, *ApJ*, **459**, 717
- Katz, J. I. 2021, *MNRAS*, **502**, 4664
- Kumar, P., Shannon, R. M., Flynn, C., et al. 2021, *MNRAS*, **500**, 2525
- Lanman, A. E., Andersen, B. C., Chawla, P., et al. 2022, *ApJ*, **927**, 59
- Levin, Y., Beloborodov, A. M., & Bransgrove, A. 2020, *ApJL*, **895**, L30
- Lewandowski, W., Kowalińska, M., & Kijak, J. 2015, *MNRAS*, **449**, 1570
- Li, D., Wang, P., Zhu, W. W., et al. 2021a, *Natur*, **598**, 267
- Li, D., & Zanazzi, J. J. 2021, *ApJL*, **909**, L25
- Li, Q.-C., Yang, Y.-P., Wang, F. Y., et al. 2021b, *ApJL*, **918**, L5
- Lu, W., Kumar, P., & Zhang, B. 2020, *MNRAS*, **498**, 1397
- Lytikov, M., Barkov, M. V., & Giannios, D. 2020, *ApJL*, **893**, L39
- Majid, W. A., Pearlman, A. B., Prince, T. A., et al. 2021, *ApJL*, **919**, L6
- Marcote, B., Nimmo, K., Hessels, J. W. T., et al. 2020, *Natur*, **577**, 190
- Margalit, B., & Metzger, B. D. 2018, *ApJL*, **868**, L4
- Massey, F. J., Jr 1951, *JASA*, **46**, 68
- Masui, K. 2017, Bitshuffle: Filter for improving compression of typed binary data, Astrophysics Source Code Library, ascl:1712.004
- McKee, J. W., Lyne, A. G., Stappers, B. W., Bassa, C. G., & Jordan, C. A. 2018, *MNRAS*, **479**, 4216
- McKinnon, M. M. 2014, *PASP*, **126**, 476
- Mckinven, R. & CHIME/FRB Collaboration 2022, ATel, **15679**, 1
- Mckinven, R., Gaensler, B. M., Michilli, D., et al. 2023, *ApJ*, **950**, 1
- Mckinven, R., Michilli, D., Masui, K., et al. 2021, *ApJ*, **920**, 138
- Merryfield, M., Tendulkar, S. P., Shin, K., et al. 2023, *AJ*, **165**, 152
- Metzger, B. D., Margalit, B., & Sironi, L. 2019, *MNRAS*, **485**, 4091
- Michilli, D., Bhardwaj, M., Brar, C., et al. 2023, *ApJ*, **950**, 134
- Michilli, D., Masui, K. W., Mckinven, R., et al. 2021, *ApJ*, **910**, 147
- Michilli, D., Seymour, A., Hessels, J. W. T., et al. 2018, *Natur*, **553**, 182
- Nimmo, K., Hessels, J., Kirsten, F., et al. 2022, *NatAs*, **6**, 393
- Nimmo, K., Hessels, J. W. T., Keimpema, A., et al. 2021, *NatAs*, **5**, 594
- Nimmo, K., Hessels, J. W. T., Snelders, M. P., et al. 2023, *MNRAS*, **520**, 2281
- Ocker, S. K., Cordes, J. M., Chatterjee, S., et al. 2023, *MNRAS*, **519**, 821
- Olausen, S. A., & Kaspi, V. M. 2014, *ApJS*, **212**, 6
- Pastor-Marazuela, I., Connor, L., van Leeuwen, J., et al. 2021, *Natur*, **596**, 505
- Petroff, E., Hessels, J. W. T., & Lorimer, D. R. 2022, *A&ARv*, **30**, 2
- Platts, E., Weltman, A., Walters, A., et al. 2019, *PhR*, **821**, 1
- Plavin, A., Paragi, Z., Marcote, B., et al. 2022, *MNRAS*, **511**, 6033
- Pleunis, Z., Good, D. C., Kaspi, V. M., et al. 2021, *ApJ*, **923**, 1
- Pleunis, Z., Michilli, D., Bassa, C. G., et al. 2021, *ApJL*, **911**, L3
- Rafiei-Ravandi, M., & Smith, K. M. 2022, *ApJS*, **265**, 62
- Rajwade, K. M., Mickaliger, M. B., Stappers, B. W., et al. 2020, *MNRAS*, **495**, 3551
- Sand, K. R., Faber, J. T., Gajjar, V., et al. 2022, *ApJ*, **932**, 98
- Scholz, F. W., & Stephens, M. A. 1987, *JASA*, **82**, 918
- Seabold, S., & Perktold, J. 2010, in Proceedings of the 9th Python in Science Conf. (Austin, TX: SciPy), 92
- Seymour, A., Michilli, D., & Pleunis, Z. 2019, DM_phase: Algorithm for correcting dispersion of radio signals, Astrophysics Source Code Library, ascl:1910.004
- Spitler, L. G., Cordes, J. M., Hessels, J. W. T., et al. 2014, *ApJ*, **790**, 101
- Spitler, L. G., Scholz, F. W., Hessels, J. W. T., et al. 2016, *Natur*, **531**, 202
- Sridhar, N., Metzger, B. D., Beniamini, P., et al. 2021, *ApJ*, **917**, 13
- Tendulkar, S. P., Gil de Paz, A., Kirichenko, A. Y., et al. 2021, *ApJL*, **908**, L12
- The HDF Group 1997–2023, Hierarchical Data Format, version5, <https://www.hdfgroup.org/HDF5/>
- The pandas development team 2020, pandas-dev/pandas: Pandas 1.1.5, v1.1.5, Zenodo, doi:10.5281/zenodo.4309786
- Tong, H., Wang, W., & Wang, H.-G. 2020, *RAA*, **20**, 142
- Trudu, M., Pilia, M., Nicastro, L., et al. 2023, *A&A*, **676**, A17
- van Haaften, L. M., Nelemans, G., Voss, R., Wood, M. A., & Kuijpers, J. 2012, *A&A*, **537**, A104
- Vedantham, H. K., & Phinney, E. S. 2019, *MNRAS*, **483**, 971
- Virtanen, P., Gommers, R., Oliphant, T. E., et al. 2020, *NatMe*, **17**, 261
- Wada, T., Ioka, K., & Zhang, B. 2021, *ApJ*, **920**, 54
- Wang, F. Y., Zhang, G. Q., Dai, Z. G., & Cheng, K. S. 2022, *NatCo*, **13**, 4382
- Xu, H., Niu, J. R., Chen, P., et al. 2022, *Natur*, **609**, 685
- Yang, H., & Zou, Y.-C. 2020, *ApJL*, **893**, L31
- Younes, G., Güver, T., Kouveliotou, C., et al. 2020, *ApJL*, **904**, L21
- Zanazzi, J. J., & Lai, D. 2020, *ApJL*, **892**, L15
- Zhang, B. 2018, *ApJL*, **854**, L21
- Zhang, Y.-K., Li, D., Zhang, B., et al. 2023, arXiv:2304.14665
- Zhao, Z. Y., Zhang, G. Q., Wang, F. Y., & Dai, Z. G. 2023, *ApJ*, **942**, 102
- Zonca, A., Singer, L., Lenz, D., et al. 2019, *JOSS*, **4**, 1298